Experimental and numerical investigation of a moored floating structure in waves

A Thesis
submitted to the Faculty of Civil Engineering
at the Norwegian University of Science and Technology
in partial fulfillment of the requirements for the degree of

Master of Science

by

Leon-Carlos Dempwolff

Abstract

Floating structures play a major role in a wide range of traditional industrial branches as well as in recently developing sectors such as renewable energies. An accurate prediction of the movement of floating structures induced by varying environmental loads is essential for their design. Numerical models nowadays play a key role in the calculation of processes in hydraulic and marine engineering, due to their advantage in cost and time efficiency. Nonetheless, the traditional approach of physical model experiments has not lost its importance since the validity of numerical tools has to be ensured. REEF3D is an open-source numerical CFD solver developed at the Department of Civil and Environmental Engineering at the NTNU. It solves the Reynolds averaged Navier-Stokes equations in two phases using a finite differences method and a level set method to capture the free surface between water and air. Floating structures are represented as a level set function, too. The motion of the function is based on the rigid body dynamics in 6DOF. A directional immersed boundary method is used to implicitly incorporate appropriate boundary conditions at the fluid-structure interface. A set of benchmark data is to be generated at the physical wave flume of the Ludwig-Franzius institute in Hanover, Germany. A simple cuboid wooden barge of constant density is examined. The motion of the barge in various waves, ranging from 2cm to 4cm in wave height and from 0.8s to 2.4s in wave period is tracked. The configuration of the set-up varies from a soft-mooring-system, ensuring free motion of the structure, to a traditional mooring system. The system includes springs of different material parameters representing the elasticity of the mooring system in a slack and a taut configuration and catenary mooring comprised of a small metal chain. The movement is quantified using an OptiTrack Motion-Tracking System composed of four cameras referencing three infra-red markers positioned on the test object. On basis of these experimental results the influence of the mooring system on the motion of the moored-floating barge is evaluated. The experimental data shall be compared to numerical data. For this purpose, the experimental set-up is reproduced in the numerical wave tank of REEF3D. A focus of the study is the investigation of the different mooring models which are available in REEF3D: an analytical approach not considering hydrodynamic forces and a quasi-static model solving the force equilibrium on a discretized line taking into account drag forces.

Contents

Abstract ii

List of figures vi

List of tables ix

List of acronyms x

List of symbols xi

1 Introduction 1
- 1.1 Motivation . . . 1
- 1.2 Operating principle of mooring lines . . . 3
- 1.3 Definition of the possible movements . . . 3
- 1.4 Potential theory . . . 4

2 Physical model tests 6
- 2.1 Experimental methods . . . 6
  - 2.1.1 Barge . . . 6
  - 2.1.2 Soft-mooring system . . . 6
  - 2.1.3 Traditional mooring system . . . 7
  - 2.1.4 The tracking-system . . . 9
  - 2.1.5 Data evaluation . . . 10
  - 2.1.6 Decay-tests . . . 10
  - 2.1.7 Tests under regular waves . . . 10
- 2.2 Experimental results . . . 11
  - 2.2.1 Depiction . . . 11
  - 2.2.2 Comparison between the traditional and the soft mooring system . . . 11
  - 2.2.3 Influence of the mooring line parameters . . . 13
  - 2.2.4 Influence of the horizontal distance between the attachment points . . . 13

3 Numerical methods **16**
3.1 Numerical approach . . . 16
3.2 Governing equations . . . 16
3.2.1 Momentum equation . . . 16
3.2.2 Continuity equation . . . 17
3.3 Turbulence treatment . . . 18
3.3.1 Direct numerical simulation . . . 18
3.3.2 Large eddy simulation . . . 18
3.3.3 Reynolds averaging . . . 19
3.3.4 Classification of turbulence closure models . . . 20
3.3.5 Two-equation models . . . 21
3.4 Computational methods . . . 22
3.4.1 General methods . . . 22
3.4.2 Requirements . . . 23
3.4.3 Finite differences method . . . 24
3.5 Implementation in REEF3D . . . 28
3.5.1 Development of the model . . . 28
3.5.2 Spatial discretization . . . 28
3.5.3 Time treatment . . . 29
3.5.4 Pressure discretization . . . 30
3.5.5 Turbulence model in REEF3D . . . 30
3.5.6 Free surface capturing . . . 31
3.5.7 Immersed boundary . . . 32
3.5.8 Parallelization . . . 32
3.5.9 Numerical wave tank . . . 33
3.5.10 Floating algorithm . . . 33
3.5.11 Mooring models . . . 35

4 Validation of the floating algorithm **39**
4.1 Set-up . . . 39
4.2 Parameter study . . . 40
4.2.1 Wave theory . . . 40
4.2.2 Tank Length . . . 41
4.2.3 Turbulence-model . . . 43
4.2.4 Mesh of the floating body . . . 44
4.2.5 Springs . . . 44
4.3 Convergence . . . 46
4.3.1 Decay-tests . . . 46
4.3.2 Regular waves . . . 48

5 Validation of the mooring models **51**
5.1 Procedure 51
5.2 Validation of the catenary mooring model 53
5.3 Validation of the quasi-static mooring model 54
5.4 Sensitivity analysis for the quasi-static system 58

6 Discussion **62**
6.1 Free-floating barge 62
6.2 Catenary mooring model 64
6.3 Quasi-static mooring model 65
6.4 Sensitivity of the quasi-static mooring model 65

7 Conclusion and Outlook **67**

References **70**

List of Figures in Appendix **74**

A Photographies of the experimental set-up **75**

B Long term time series **80**

List of Figures

1.1 Definition of the six degrees of freedom 4

2.1 Sketch of the experimental set-up for the soft-mooring configuration [Meyer (2018)] 7
2.2 Sketch of the experimental set-up for the traditional mooring configuration (chain and taut) 8
2.3 Movement under different mooring configurations in the experiment (T=0.8 s, H = 3cm) 11
2.4 Movement under different mooring configurations in the experiment (T=1.2 s, H = 3cm) 12
2.5 Movement under different mooring configurations in the experiment (T=1.6 s, H = 3cm) 12
2.6 Movement of the barge in the experiment with different rope mooring parameters (T = 1.2 s, H = 3cm) 13
2.7 Movement of the barge in the experiment with different attachment points at the floor (T = 1.2 s, H = 3cm) 14
2.8 Movement of the barge in the experiment with different attachment points at the floor (T = 1.6 s, H = 3cm) 14

3.1 Demonstrative eddy structure in a flow(left) and time dependency of a velocity component in a fixed point(right) [Ferziger and Perić (2008)] 18
3.2 Turbulence averaging for a stationary flow (left) and an instationary one (right) [Ferziger and Perić (2008)] 19
3.3 The different spatial discretization on a generic example for 1D [jr. Oertel et al. (2015)] 25
3.4 Illustration of stability problems on a diffusion/convection problem [Griebel et al. (1998)] 26
3.5 The four schemes for time discretization presented, from left to right: Explicit Euler, Implicit Euler, trapezoidal rule, midpoint rule [Ferziger and Perić (2008)] 27
3.6 A staggered grid [Griebel et al. (1998)] 32
3.7 Catenary mooring model 36
3.8 Discretization of the mooring lines [Martin et al. (2018*b*)] 37

3.9 Force equilibrium on a single node $P^{(j)}$ 38

4.1 Sketch of the barge in the numerical wave tank 39
4.2 Contour of the level set function describing the boundary to the solid body ($\Delta x = 0.005m$) 40
4.3 Three different wave theories and experimental test compared in an empty tank, T=0.8 H=3cm 41
4.4 Decay-test for two different tank lengths compared to the experimental data 42
4.5 Regular waves for two different tank lengths (T = 1.6s, H = 3cm) . . 42
4.6 Comparison of the $k-\omega$-turbulence model with the potential solution (T = 1.6 s, H = 3 cm) 43
4.7 Comparison of the movement in regular waves for three different meshes for the floating body ($\Delta x = 0.005m$ T=0.8s H=3cm) 44
4.8 The movement of the body with and without springs ($\Delta x = 0.005m$, T= 0.8 s, H = 3 cm) 45
4.9 The movement of the body with and without springs ($\Delta x = 0.005m$, T= 1.2 s, H = 3 cm) 46
4.10 The movement of the body with and without springs ($\Delta x = 0.005m$, T= 1.6 s, H = 3 cm) 47
4.11 Comparison of the decay-test for three mesh resolutions 47
4.12 Comparison of three mesh resolutions, T=0.8s H=3cm 49
4.13 Comparison of three mesh resolutions, T=1.2 s H=3cm 49
4.14 Comparison of three mesh resolutions, T=1.6 s H=3cm 50

5.1 Initial position of the floating barge and the mooring chains 53
5.2 Movement of the barge using a catenary mooring model compared to experimental results (T = 1.2 s, H = 3cm) 53
5.3 Movement of the barge using a catenary mooring model compared to experimental results (T = 1.6 s, H = 3cm) 54
5.4 Initial position of the floating barge and the mooring ropes of a slack configuration 55
5.5 Initial position of the floating barge and the mooring lines of a taut configuration 55
5.6 Movement of the barge using a quasi-static mooring model compared to experimental results (slack)(T = 1.2 s, H = 3cm) 56
5.7 Movement of the barge using a quasi-static mooring model compared to experimental results (slack)(T = 1.6 s, H = 3cm) 56
5.8 Movement of the barge using a quasi-static mooring model compared to experimental results (taut, F2)(T = 1.2 s, H = 3cm) 57

5.9 Movement of the barge using a quasi-static mooring model compared to experimental results (taut, F2)(T = 1.6 s, H = 3cm) 57
5.10 Movement of the barge using a quasi-static mooring model and the spring model compared to experimental results (taut, F2)(T = 1.2 s, H = 3cm) 59
5.11 Movement of the barge using a quasi-static mooring model for two different values of EA compared to experiments (taut, F2)(T = 1.2 s, H = 3cm) 60
5.12 Movement of the barge using a quasi-static mooring model for two different line lengths compared to experiments (taut, F2)(T = 1.2 s, H = 3cm) 60
5.13 Movement of the barge using a quasi-static mooring model for different vertical positions of the attachment points on the box (taut, F2)(T = 1.2 s, H = 3cm) 61

List of Tables

2.1 Overview over the tested configurations 9
2.2 Overview over the tested waves 10
2.3 Overview of the parameters of the examined waves 11

3.1 Classification of turbulence models [Laurien and Oertel (2018)] 20

List of acronyms

CFD Computational fluid dynamics

CFL Courant-Friedrich-Levy

DNS Direct numerical simulation

FSI Fluid structure interaction

LED Light emitting diode

LES Large eddy simulation

MPI Message passing interface

NS Navier-Stokes

RANS Reynolds averaged Navier-Stokes

RAO Response amplitude operators

SPH Smoothed particle hydrodynamics

TVD Total variation diminishing

List of Symbols

A	Cross-section area
c_t	Drag coefficient in tangential direction
c_n	Drag coefficient in normal direction
c	Spring constraint
d	Waterdepth
δ_{ij}	Kronecker delta
ϵ	Turbulent dissipation
E	Young's modulus
f_{ext}	External forces
$\vec{f}$	Tangential unit vector of the cable
F_h	Horizontal force
F_H	Hydrodynamic forces
F_T	Cable tension force
g_i	Gravity acceleration
γ_0	Cable mass per unit length
Γ	Interface between the phases
I	Moment of Inertia
J^{-1}	Rotational matrix
k	Kinetic energy
κ	Constant of 0.4
λ	Wave length
L	Length of the mooring line
M	Acting moments
ν	Viscosity
ν_t	Turbulent viscosity
ω	Specific turbulent dissipation
ω_s	Specific turbulent dissipation at the free surface
Ω	Surface of the floating body
p	Pressure
ϕ	Level set function or Euler angle
ψ	Euler angle
ρ	Density
r	Position vector of the cable
R	Distance to the center of gravity
s	Cable coordinate
S	Mean rate of strain
$S(\Phi)$	Smoothed sign function
t	Time

τ	Shear tension
θ	Euler angle
u	Velocity in x direction
u_i	Velocity-tensor
$\tilde{u}$	Convection velocity
v	Velocity in y-direction
w	Velocity in z-direction
x_i	Coordinate tensor
$\tilde{x}$	Dimensionless parameter for length of absorption/generation zone
y_*	Distance from the nearest wall
y'	Virtual origin of the turbulent length scale

Chapter 1

Introduction

1.1 Motivation

In a wide range of practical applications floating structures play a major role. As of now more than a fourth of the world's oil and gas production comes from offshore (Agency (2018)). In addition, there are many arising industrial branches that rely on floating bodies. Staying in the energetic sector, renewable energies are projected to be produced offshore, with offshore wind energy platforms being constructed in deeper seas of more than 50m depth (Bento and Fontes (2019)). Other concepts rely on the use of wave energy to convert into electric energy (Blažauskas et al. (2015)). In Norway a large export industry is salmon production from aquacultures, with expected growth rates in the upcoming years (Ernst and Young (2017)). But not only fish, even seaweed is cultivated in aquaculture farms (Sulaiman et al. (2013)). All these structures have in common that they need to be kept in place for reliable operation. This is done by mooring lines attaching the floating structure to the sea floor. Various concepts exist including a wide range of materials and arrangements.
While the large structures for the oil and gas industry have traditionally been calculated using potential-theory, the smaller scale structures emerging a more accurate calculation is desirable regarding the safe but also economic design of the structures. Furthermore mooring lines can be an important factor for the function of the floating structure such as presented in Fitzgerald and Bergdahl (2008), further illustrating the need for a precise calculation.
Numerical simulations are a valuable tool in many disciplines, also established in the field of marine engineering. They are able to reduce the cost and time caused by physical simulations. The methods are evolving quickly and the computational power available is increasing. But in order to generate reliable results, the solvers need to be validated carefully to ensure they represent the real world properly.
Typical experimental set-ups include complex geometries for floating bodies repre-

senting scaled equivalents of real floating bodies to be applied on the ocean. For the validation of numerical tools, it is desirable to start with simpler geometries. Only if their behaviour is represented correctly, the integration of more complex solid bodies is an option.
No matter the importance of this simple data, it is usually difficult to obtain. One set of benchmark-data available for a very simple barge stems from Ren et al. (2015), but its reduction to just one wave reduces the possibilities of validation. A typical application of a rather simple floating body is a floating breakwater. Here several physical experiments were undertaken to estimate the movement under waves. The influence of various parameters was examined. These are for the example the use of pneumatic chambers in He et al. (2012), the use of different geometries, including mesh and other porous elements in Ji et al. (2016), the use of horizontal plates in Christensen et al. (2018) or different attachment points in Sannasiraj et al. (1998). But either important parameters of the floating structure are not known or their complexity makes them unnecessarily difficult to implement as a validation case. Hydrodynamic forces on isolated mooring lines are also tested in experiments, as for example in Bergdahl et al. (2016), but still no tests for a very simple geometry combined with exactly controlled mooring line parameters was found.
As a consequence, a dataset especially considering these requirements was to be generated within this thesis, extending an existing dataset for a free floating barge to allow for the validation of the floating-algorithm of the Computational fluid dynamics (CFD)-solver REEF3D and the mooring models included. The experimental procedure is introduced in chapter 2 and results for different configurations are shown.
The advantages of CFD are already pointed out. However, it is a method relying on numerous models, approximations and simplifications. It is therefore indispensable for the user to critical evaluate on the output of the model. Hence, profound knowledge of the underlying concepts of the solver is necessary to apply it effectively. On the other hand entire books are filled introducing mathematical descriptions, discretization methods and solution methods for the generated equations, so that it would exceed the possibilities of this thesis to cover them all in detail. As a consequence just the mathematical description of the problem is introduced, including the treatment of turbulence, the different discretization schemes are pointed out, as well as some criteria to evaluate the quality of the model before introducing the main idea of the applied discretization scheme in chapter 3.
The results for the free floating barge are then presented in chapter 4 and compared against the experimental data, before introducing the mooring systems in chapter 5. The results are discussed in chapter 6. Concluding remarks and prospects for further research are then given in chapter 7.

1.2 Operating principle of mooring lines

Mooring chains or cables, that are conventionally used, have completely different mechanisms of providing station keeping of a floating body than synthetic ropes do. Chains provide a restoring force dependent on the part of it, that is lifted from the floor. The more the platform is displaced the more of the chain is lifted from the floor and the larger the restoring force caused by its own weight gets (Brown (2005)). The elasticity of such a mooring cable is only activated in the case of extreme conditions (Faltinsen (1990)).
Due to the large weight of this traditional mooring system, synthetic mooring lines are recently of increasing interest. They are typically taut, but avoid shock loads on the floating body due to their elasticity. The weight is reduced to one tenth, compared to a steel mooring, so that their application is especially interesting in deep water locations (Brown (2005)).
To be able to include both of these mechanisms in the numerical solver, validation data for both types of mooring lines is generated. A mooring system typically consists of several mooring lines, spread in different orientations. Also, additional elements such as buoyancy elements or additional weights or interconnections between mooring lines can be part of the system. Again the aim is to keep the validation data as simple as possible, so no such elements are included in the tests.

1.3 Definition of the possible movements

Any body in space has six degrees of freedom in which to move. Consequently the same possible motions also account for a floating barge. Those are three translational movements along the axes, and three rotational movements around the axes. The naming of the motions sometimes differs a little in literature, so a definition is given here, to avoid any confusion following M J Journée and W Massie (2001). In the current application the x-axis, is given oriented in the direction of the wave tank, the y-axis as crosswise to it and the z-axis as vertical. An illustration is found in Figure 1.1.

Surge (x_b) Translational movement in x-direction

Sway (y_b) Translational movement in y-direction

Heave (z_b) Translational movement in z-direction

Roll (Φ) Rotational movement around the x-axis

Pitch (Θ) Rotational movement around the y-axis

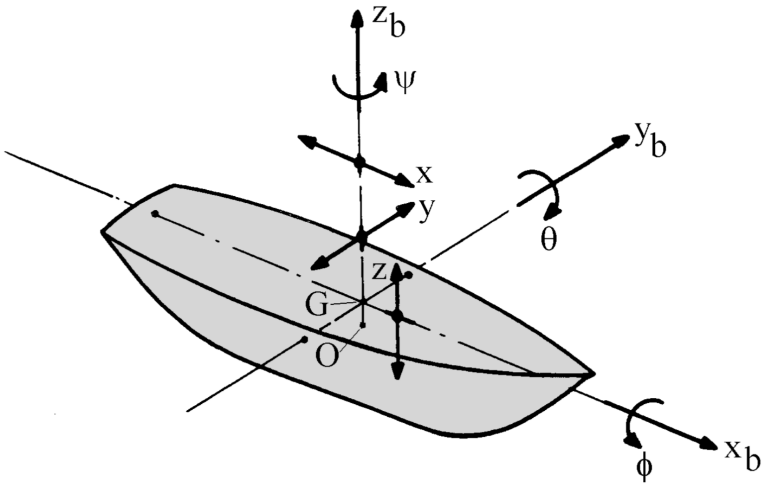

Figure 1.1: Definition of the six degrees of freedom

Yaw (Ψ) Rotational movement around the z-axis

In two dimensions this is reduced to just three degrees of freedom. In a plane within the x- and z-axis, this is just the surge, heave and pitch motion.

1.4 Potential theory

Besides experimental and numerical approaches a third concept for the calculation of the motion response in waves should also be mentioned. These are approaches relying on the potential theory, for example given in M J Journée and W Massie (2001). It is an approach relying on a simplified set of equations compared to the Navier-Stokes (NS) equations introduced in section 3.2, that even allows for an analytical solution in simple cases. The mathematical description of the problem makes it necessary to introduce several assumptions. It is not the focus here, but same basic concepts are given in the following, to show where the limitations are.
A potential function is introduced, that has no physical meaning, but its derivative leads to the velocity vector (Faltinsen (1990)):

$$V = i\frac{\partial \Phi}{\partial x} + j\frac{\partial \Phi}{\partial y} + k\frac{\partial \Phi}{\partial z}, \tag{1.1}$$

where i,j and k are unit vectors.
In order to apply the theory two criteria have to be met:
The flow is free from rotation, that means all forces acting upon a particle are normal to its surface (Durst (2006)).

The second criteria is, that since water is incompressible the Laplace equation needs to be fulfilled:

$$\frac{\partial^2 \Phi}{\partial x^2} + \frac{\partial^2 \Phi}{\partial y^2} + \frac{\partial^2 \Phi}{\partial z^2} = 0. \tag{1.2}$$

To solve these equations a set of boundary-conditions needs to be introduced. They can be found for example in Faltinsen (1990). For an isolated water body this results in the linear wave theory. This can now be used to incorporate the forces acting on the body.

The motion of the body can be superimposed from different force components. This is also done to calculate the motion in response to irregular waves. For a body in regular waves two components are differentiated. These are the forces acting on a moving body in still water and the forces induced by the oscillating water. For an isolated heave motion, often used as an academic example (M J Journée and W Massie (2001)), the body can now be described as a spring system, where the elastic and damping components are determined analytically. The main assumptions, that need to be made, are that the waves are not affected by the floating structure. Diffraction is not taken into account, and the body is assumed to be small in comparison to the wave, so that the force acting on the body's bottom is constant. The advantage compared to the approach introduced in this thesis is, that it is very effective.

In a case like the one presented in chapter 2 those assumptions are not really met, but still with the rather gentle waves generated, the solution should not be too distant. However, the idea of the solver is to have a tool that is able to handle a wide variety of cases and not to rely on the same assumptions that have to be made in order to find an analytical solution.

Chapter 2

Physical model tests

2.1 Experimental methods

2.1.1 Barge

The tests were performed at the wave flume of the Ludwig-Franzius-Institute in Hanover. The flume has a length of 110m and a width of 2.2m. It is equipped with a piston-type wave maker. The barge consists of massive wood, leading to a uniformly distributed mass. In order to prevent the material from swelling, it is sealed using three layers of varnish coating. The dimensions of the box are $0.6m \cdot 0.3m \cdot 0.15m$, which results in a total volume of $0.0027m^3$, with a weight of $18.35kg$. This results in a density of $\rho = 680kg/m^3$. On top of it four eye screws were placed to provide the possibility to perform decay-tests, as well as two ones on the front and back at the height of the waterline for attaching the mooring system, and one on the center of each lateral side for attaching the soft-mooring system. A photography of this body is given in the appendix.
The water level was chosen to 0.85 m for all experiments conducted. Two different data sets were used for the validation of the numerical model. The one for the soft-mooring system was generated in Meyer (2018), while the data for the set-ups including a traditional mooring system were generated in the framework of this thesis.

2.1.2 Soft-mooring system

Two basic set-ups for the mooring system were chosen. The first one was a soft mooring system, allowing for unhindered movement in pitch-direction, due to its attachment point at the rotational axis. In the heave direction the influence of the soft mooring-system is negligible, due to the orientation of the springs orthogonal to the axis of motion. In Meyer (2018), it is shown, how small the influence of this

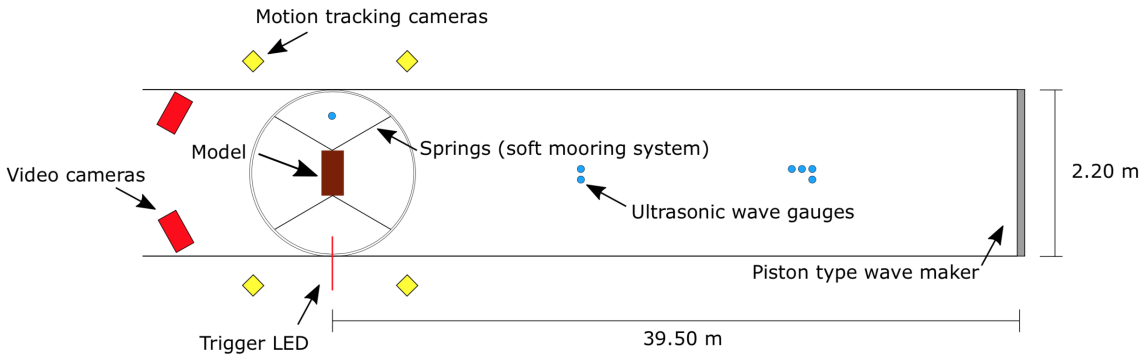

Figure 2.1: Sketch of the experimental set-up for the soft-mooring configuration [Meyer (2018)]

system is. It was implemented using an aluminium ring that surrounded the model and was fixed to the wall of the flume. The ring and the lateral sides of the barge were connected via a set of springs within an angle of 60° to the incident wave direction. For each connection two springs with a constant of 10 N/m were placed into series, resulting in a final stiffness constant of 5 N/m. In Figure 2.1, a sketch of this set-up can be seen.
The barge was moored in a distance of 39.5m to the wave maker, in order to establish a time-window of movement unaltered from reflecting waves returning from the flume's end, and also to reduce the length that has to be modelled by the numerical code. For this set-up a total of seven ultrasonic wave gauges was used. Six of them were positioned in a row in front of the barge and one was used next to it. This is the dataset of Meyer (2018).

2.1.3 Traditional mooring system

The second basic set-up consisted of the same barge moored by a traditional mooring system. Different materials for the mooring lines were chosen. The two main classes are a rope mooring system and a small metal chain partly laying on the floor. For the rope mooring four stiff polyethylene-ropes were connected to attachment-points at the floor of the flume. Those points were weight ballasted. The top of the attachment points was 12.5 cm above the floor. The material is very stiff, so that it is assumed to stretch only negligibly under the given loads. To exactly control the elasticity of the mooring system, to account for the stretch within real applications and to avoid shock loads, the connection to the barge was established, via a set of springs. Three different sets of springs with elasticity-constants of 0.072N/mm (F1), 0.209N/mm (F2) and 0.305N/mm (F3) were used. For all of the constants a horizontal distance

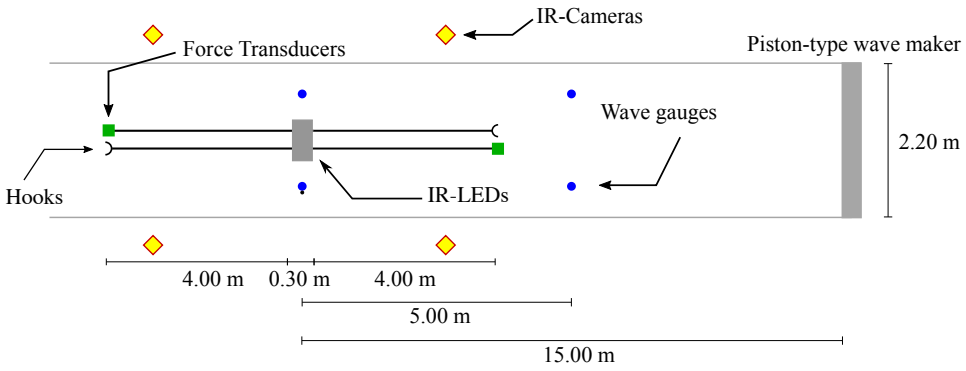

Figure 2.2: Sketch of the experimental set-up for the traditional mooring configuration (chain and taut)

of 8.30 m between the attachment points was examined, that is 4 m distance from each side of the box. In order to allow for the change of the springs, the connection was established via a set of two key rings on each mooring line. The length of the line was chosen to 3.97 m, so that the diagonal length including the springs and the key rings cumulated to 4.07 m. This matched exactly with the diagonal length between the attachment points. The density of the rope material is with $\rho = 0.97 g/cm^3$ a little lower than the one of water so that it creates some buoyancy. Due to the use of the metal key rings and the springs, no such behaviour could be observed.
On the attachment points the forces exerted on the mooring lines were measured using force sensors. Due to the fact that the system was symmetric and the long drying periods for the sensors, of which only a limited amount was available, only one side in front of the barge and one side behind it were measured. A sketch of this set-up is depicted in Figure 2.2.
In addition, a slack configuration was also tested. The same mooring lines with the spring F1 were used, but the attachment points at the floor were moved closer to each other. The horizontal distance in between was then only 7.90 m. The length of the mooring lines were left unchanged.
The second system consisted of four metal chains with a length of 4.23 m and a weight per unit length of 0.023 kg/m, that connected the box to attachment points, the same way as described above. The horizontal distance between the attachment points on the sea floor was the same as in the taut configuration, so that the chain partly lay on the bottom. Therefore, it was not possible to measure the forces here. Due to the fact that no properties of any prototype had to be met, the choice of material was done following the availability in the retail market. A summary of the tested

Table 2.1: Overview over the tested configurations

Parameter	**Soft-mooring**	**Traditional mooring**				
Line material	Horizontal springs	Chain ($\rho = 7.85\frac{g}{cm^3}$ $\gamma_0 = 0.023\frac{kg}{m}$)	Polyethylene rope + springs ($\rho = 0.97\frac{g}{cm^3}, d = 1.5mm$)			
Distance anchoring points		8.30 m	8.30 m (Taut)			7.90 m (Slack)
Length of the line		4.23 m	4.07 m			
Spring used			0.072 N/mm (F1)	0.209 N/mm (F2)	0.305 N/mm (F3)	0.072 N/mm (F1)

configurations and the parameters of the material is given in Table 2.1.
The model was positioned in 15 m distance to the wave-maker. For this set-up only four ultrasonic wave-gauges were used. Two of them were positioned next to each other in front of the barge, and two of them positioned on each side of the barge.

2.1.4 The tracking-system

An OptiTrack-system was used, to measure the barge's movement in reaction to the waves. It consists of four infra-red cameras, located in the four corners around the barge. On top of the barge, three infra-red-LEDs were positioned, powered by a battery-pack. The aim of the use of active markers was to avoid problems due to reflections of the infra-red light on the water surface, which would have occurred using passive markers. Additionally to the infra-red cameras, a traditional video-camera was installed for visualization of the movement.
Considering the specific local conditions and the position of the measurement PC, all sensors were connected to two HBM Quantum measurement amplifiers. These were synchronized using a trigger in form of a battery-pack connected to the amplifiers as well to an additional Light emitting diode (LED) mounted on the side of the flume, where it could be registered by all of the cameras. Switching on the trigger led to an electric tension, registered on the amplifiers and also switching on the LED.

Table 2.2: Overview over the tested waves

wave-height [cm]	**wave-period [s]**					
2		1			1.6	
3	0.8	1	1.2	1.4	1.6	1.8

2.1.5 Data evaluation

The resulting data was analysed in use of the program MATLAB, as presented in Meyer (2018). Both, the wave gauge data and the motion-tracking data were preprocessed using a low-pass filter to remove high frequency-oscillations as well as noise. The data series was cut according to the time the trigger-LED was visible and the movement calculated according to the position of the center of gravity and the rotation.

2.1.6 Decay-tests

In order to capture the movement of the body undisturbed from waves, several decay-tests were performed. These consist of an evaluation of the movement without external wave forces. The barge is displaced and the motion until it returns to its equilibrium position is tracked.
Two different kinds of decay-tests were performed, one for the heave movement and one for the pitch movement. For the heave-test, the body was lifted via a rope, which was then cut. For the pitch decay test a person had to enter the flume and press on one edge to induce a rotation to the body. After the water was still the body was released.

2.1.7 Tests under regular waves

For the tests under regular waves, each mooring configuration was exposed to a set of seventy waves in a row, with the same parameters. After the water reached a still status again the parameters were altered. Each configuration was tested under the influence of eight different waves shown in Table 2.2. In this thesis no Response amplitude operators (RAO) are generated, but the exact time series of the movement of the barge is compared. Therefore three waves were chosen displaying the whole range of the periods tested, for further examination. The ones picked have a period of 0.8 s, 1.2 s and 1.6 s, all with a height of 3 cm.

Table 2.3: Overview of the parameters of the examined waves

Period: / Parameter:	0.8 s	1.2 s	1.6 s
wavelength [m]	0.999	2.213	3.604
wave number	6.290	2.839	1.7434

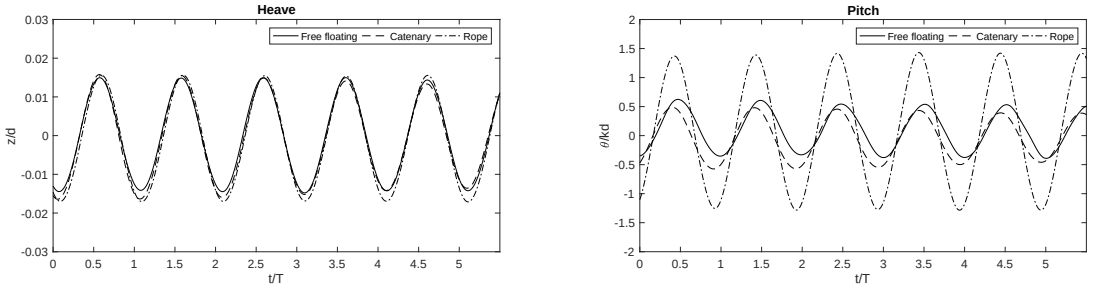

(a) (b)

Figure 2.3: Movement under different mooring configurations in the experiment (T=0.8 s, H = 3cm)

2.2 Experimental results

2.2.1 Depiction

In the following the focus is just on the influence of the mooring systems compared to the soft-mooring system and the influence of the different parameters of the traditional mooring system, since the observations on the movement the soft-moored barge are already given in detail in Meyer (2018). All plots are dimensionless using the wave period F_T for normalizing the time, the water depth d to normalize the translational movements and the wave number k times water depth d to for the rotational movements. To allow for an idea of the absolute values of the movements, the numbers are given in Table 2.3. The windows were chosen in such a way, that the heave phase of the experiments matches.

2.2.2 Comparison between the traditional and the soft mooring system

In Figure 2.3 to Figure 2.5, the behaviour of the body under different waves can be seen for the soft-moored system, the taut rope-mooring with spring F2 and the chain. A similar influence of the mooring-system under all the waves can be observed. The heave motion is only slightly affected with an increase of amplitude with the chain

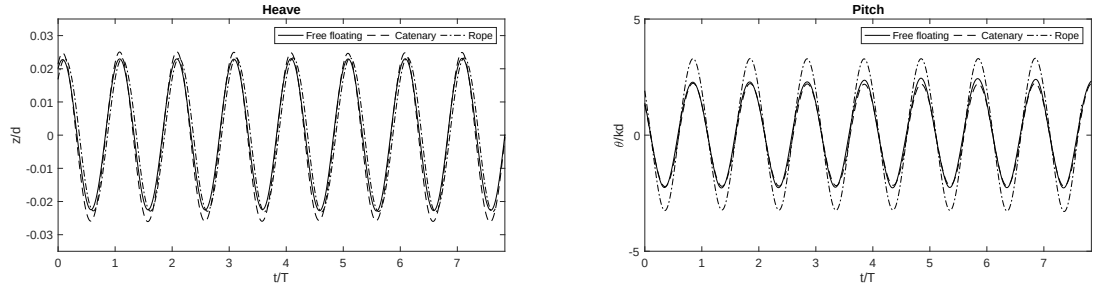

(a) (b)

Figure 2.4: Movement under different mooring configurations in the experiment (T=1.2 s, H = 3cm)

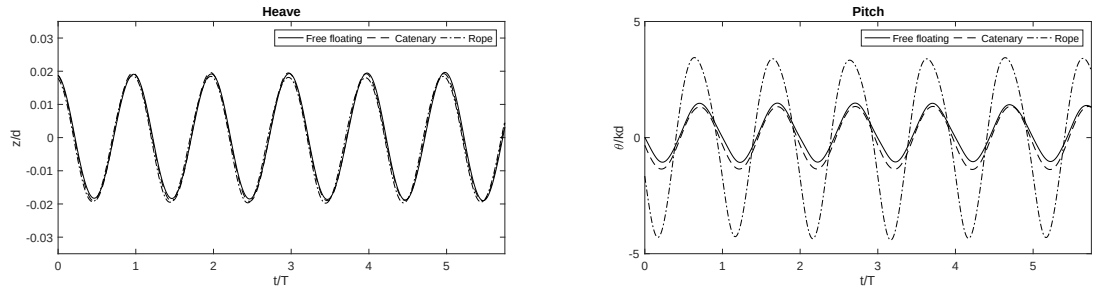

(a) (b)

Figure 2.5: Movement under different mooring configurations in the experiment (T=1.6 s, H = 3cm)

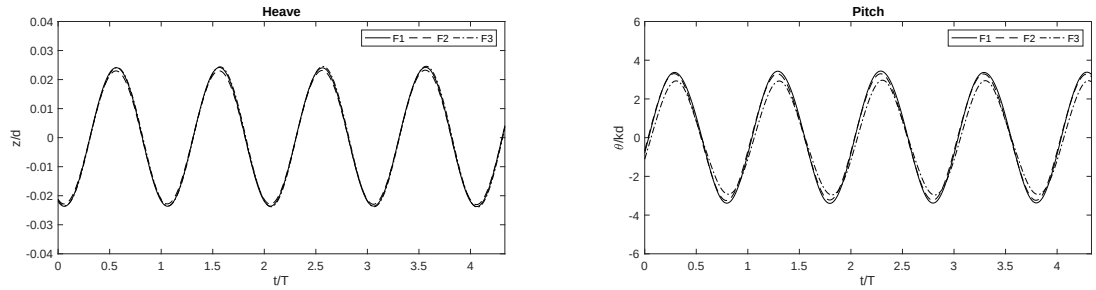

(a) (b)

Figure 2.6: Movement of the barge in the experiment with different rope mooring parameters (T = 1.2 s, H = 3cm)

mooring applied, for the waves with a period of 0.8s and 1.2s. The rope mooring does not show any influence on this motion.
In contrast, the influence on the pitch motion is enormous with an increase of the amplitude of more than twice for waves T = 0.8 s and T = 1.6 s. For waves with a period of 1.2 s, the increase is not that high but still significant. The chain mooring has only a small influence on this movement. For the shortest wave, a phase lag compared to the free-floating barge can be observed, while for the largest wave some lower troughs can be observed. On the waves with T = 1.2 s, no influence can be observed at all.

2.2.3 Influence of the mooring line parameters

In the following the three different spring constants, are compared against each other in regular waves with a period of 1.2s and H=3cm. Again it can be seen, that the influence on the heave motion is minimal, but the different mooring-line configurations lead to different pitch movements. The smallest motions are observed using the stiffest spring F3, and the largest amplitudes can be seen with the most flexible spring F1 used. The movement for spring F2 lies in between the two. The difference in amplitude is not excessively large with 2.8 for spring F3 and 3.4 for spring F1.

2.2.4 Influence of the horizontal distance between the attachment points

It can be seen, that the slack mooring configuration shows almost the same motion as the soft-moored one in a wave of 1.2 s (Figure 2.4). The heave amplitude is a little increased, leading to higher values than for the soft-moored and the tense-moored configuration. The peak-values of the pitch motion are also increased, but

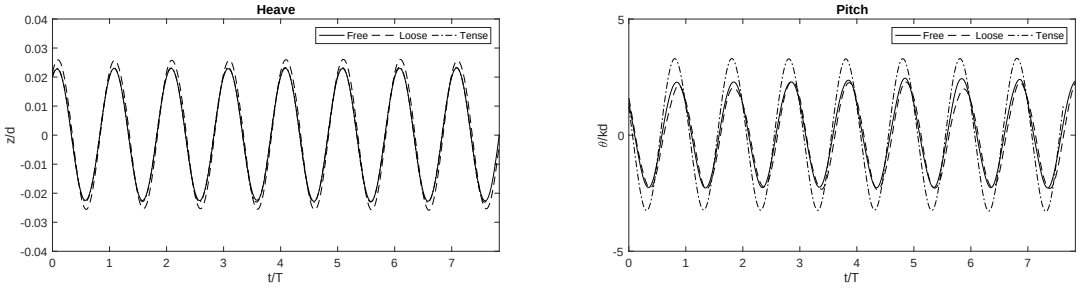

(a) (b)

Figure 2.7: Movement of the barge in the experiment with different attachment points at the floor (T = 1.2 s, H = 3cm)

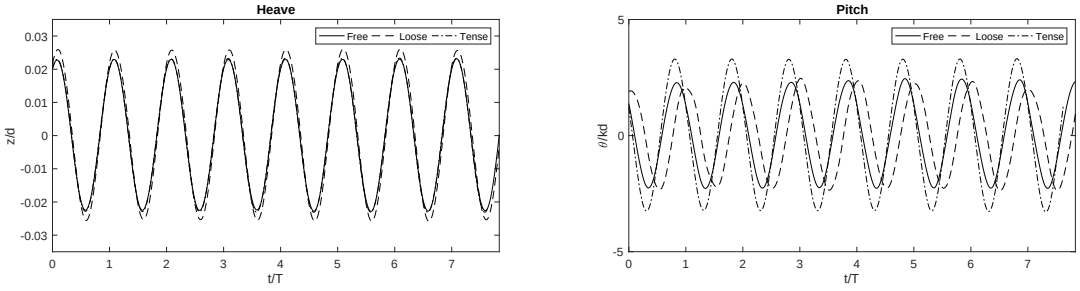

(a) (b)

Figure 2.8: Movement of the barge in the experiment with different attachment points at the floor (T = 1.6 s, H = 3cm)

still significantly lower than for the taut mooring-configuration. The troughs match with the soft-moored configuration. The pitch motion of the tense mooring system lags compared to the one of the other two motions.
For a wave of 1.6 s (Figure 2.8), the influence is similarly small. No difference in the heave motion of the experiments can be observed, but the pitch motion also shows some lag in the phase. The troughs in the pitch motion of the slack configuration are slightly reduced compared to the free-floating one.

Chapter 3

Numerical methods

3.1 Numerical approach

Two ways of describing the mechanics of a fluid are established. These are the Lagrangian point of view and the Eulerian one. The Lagrangian one is based on a viewing point, that moves with the fluid (Laurien and Oertel (2018)). This concept is underlying to an numerical approach called Smoothed particle hydrodynamics (SPH). Recently this idea got some attention (see for example Ren et al. (2015)). The method has some advantages like the capturing of the free surface, but a major problem is the definition of boundaries at the interface between solids and the fluid.
The Eulerian point of view instead, is fixed while the fluid moves relative to it. It is then used to examine the flows passing through a fixed volume of control (Laurien and Oertel (2018)). This is the more common approach in CFD, and also used in REEF3D.

3.2 Governing equations

3.2.1 Momentum equation

Numerical simulations of flow are used in many disciplines. They are all based on the same principles and mathematical approaches. However, the properties of the models and the questions arising are different in marine engineering, than in other disciplines. As a result the focus is just on the equations important for this thesis and the more general fundamentals are not mentioned.
The mathematical description of the flow is given by the NS-equations. In the given range of applications the solver just treats fluids that are viscous, but the range of the Mach number, that sets the velocity in relation to the speed of sound, allows the assumption of an incompressible flow. The governing equations for three dimensions

are composed of four equations: the momentum equation for each coordinate direction and in addition the continuity equation, based on the conservation of mass is introduced.
There are various ways of derivating the NS equations. This summary is following jr. Oertel et al. (2015). The momentum equation is formed as the sum of all momentums entering the control volume, the ones leaving the control volume, the tensions acting on it and the forces acting upon the mass. For the mass we will restrict to the forces of gravity. The pressure of the fluid is acting upon all the sides of the boundaries is the normal stress. Including it in the equation leads to a term of its space derivative for each equation. The shear and normal tensions depend upon the flow properties of the fluid. Applying Newton's second law, this leads to a description of the resulting forces depending on the derivatives of the velocities and the viscosity ν.
Finally, this results in the complete NS-equations for an incompressible fluid, presented in compact tensor notation (Laurien and Oertel (2018)):

$$\frac{\partial u_i}{\partial t} + u_j \frac{\partial u_i}{\partial x_j} = -\frac{1}{\rho}\frac{\partial p}{\partial x_i} + \nu \frac{\partial}{\partial x_j}\left(\frac{\partial u_i}{\partial x_j} + \frac{\partial u_j}{\partial x_i}\right) + g_i \tag{3.1}$$

The discretization of the different terms in the equation differs, so a short overview of the components should be given. On the left hand side, there is a transient term dependent on the time and a convective term formed depending on the first derivative in space. On the right hand side, there is a pressure term, a diffusive term, smoothing out gradients and accounting for the energy consumption in a real fluid and a source term that just includes gravity in this context.

3.2.2 Continuity equation

Additionally to the conservation of momentum, the conservation of mass has to be ensured. In a similar way as for the momentum, the resulting flows over the boundaries of the volume can be balanced. For a detailed summary again see jr. Oertel et al. (2015). For an incompressible fluid this results in:

$$\frac{\partial u}{\partial x} + \frac{\partial v}{\partial y} + \frac{\partial w}{\partial z} = 0 \tag{3.2}$$

or in tensor notation:

$$\frac{\partial u_i}{\partial x_i} = 0. \tag{3.3}$$

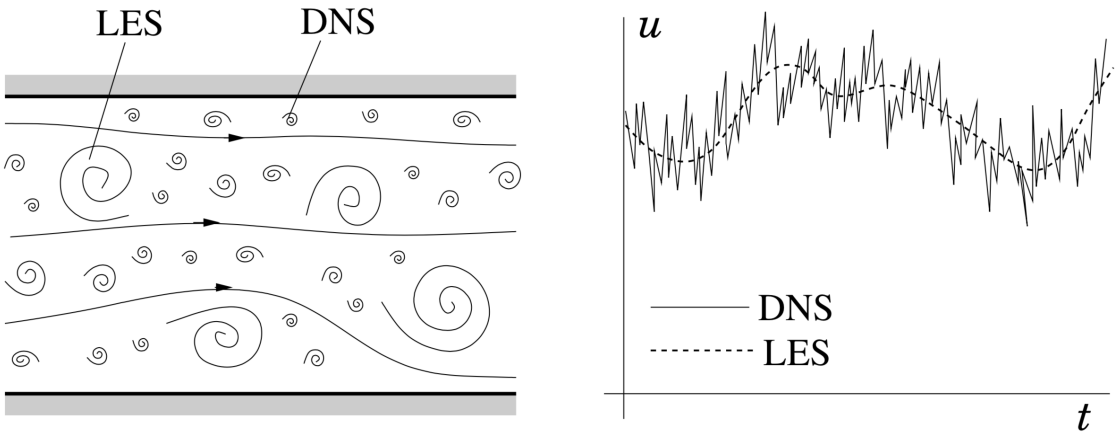

Figure 3.1: Demonstrative eddy structure in a flow(left) and time dependency of a velocity component in a fixed point(right) [Ferziger and Perić (2008)]

3.3 Turbulence treatment

3.3.1 Direct numerical simulation

With these equations it is already possible to compute an exact solution for the processes in a fluid. There are four equations now for the four unknown variables u, v, w and p. Due to the turbulent nature of the flow in typical applications, the scale of the resolution in space and time needs to be very fine in order to include the whole energy-cascade. This makes the calculation extremely demanding and requires high computational capacities. This method known under the name Direct numerical simulation (DNS) is therefore mainly used in basic research or for the validation of other numerical methods.

3.3.2 Large eddy simulation

A widely used method to reduce the computational cost, is the Large eddy simulation (LES). Here, only the largest eddies are simulated, while the smaller ones are modelled making use of the self similarity of the turbulence structures both in space and time. An illustration of the eddy structure in a flow and the resulting simplifications can be seen in Figure 3.1. The basis for this method are filtered versions of the NS equations. Details can for example be found in Ferziger and Perić (2008). Despite the reduction of the computational expenses, calculations are still quite demanding, while the results are more precise than required in many applications.

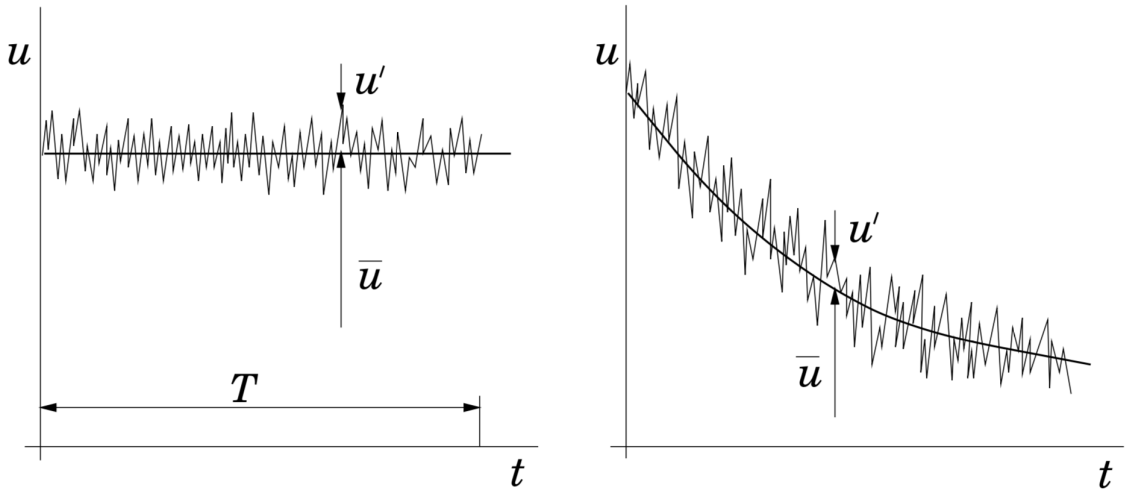

Figure 3.2: Turbulence averaging for a stationary flow (left) and an instationary one (right) [Ferziger and Perić (2008)]

3.3.3 Reynolds averaging

In typical engineering applications the user is not interested in knowing all the parameters of a turbulent flow. Usually it is enough to know about the influence of the eddies on the mean flow in form of the energetic consumption they induce. Hence, approximations are introduced to the NS-equations to further reduce the computational cost. In the process of Reynolds averaging the equations all variables depending on time are split into an averaged one $\bar{\phi}$ and a fluctuating one ϕ' according to (Ferziger and Perić (2008)):

$$\phi = \bar{\phi} + \phi' \tag{3.4}$$

with:

$$\bar{\phi} = \frac{1}{\delta t} \int_{\delta t} \phi dt \tag{3.5}$$

and:

$$0 = \frac{1}{\delta t} \int_{\delta t} \phi' dt \tag{3.6}$$

An illustration of this step is given in Figure 3.2. Replacing all parameters of the NS equations with the averaged and fluctuating one leads to the Reynolds averaged Navier-Stokes (RANS) equations. Since the average of the fluctuations is zero by definition, the linear components of the equation velocity, pressure and friction are replaced by the averaged ones. For the quadratic nature of the diffusive terms, the fluctuating component is not averaged to zero but additional terms of correlation be-

tween the components of the fluctuating velocities arise (Laurien and Oertel (2018)). These so called Reynolds tensions are summarized to a tensor:

$$\tau_{ij} = -\rho \begin{pmatrix} \overline{u'u'} & \overline{u'v'} & \overline{u'w'} \\ \overline{v'u'} & \overline{v'v'} & \overline{v'w'} \\ \overline{w'u'} & \overline{w'v'} & \overline{w'w'} \end{pmatrix} \tag{3.7}$$

Including this tensor in the NS-equations leads to the RANS equations.

$$\frac{\partial \bar{u}_i}{\partial x_i} = 0 \tag{3.8}$$

$$\frac{\partial \bar{u}_i}{\partial t} + \bar{u}_j \frac{\partial \bar{u}_i}{\partial x_j} = -\frac{1}{\rho}\frac{\partial \bar{p}}{\partial x_i} + \frac{\partial}{\partial x_j}\left(\nu\left(\frac{\partial \bar{u}_i}{\partial x_j} + \frac{\partial \bar{u}_j}{\partial x_i}\right) - \overline{u_i' u_j'}\right) + g_i \tag{3.9}$$

Due to the introduction of the new fluctuating components, the number of unknown variables exceeds the number of equations to determine them. In order to overcome this so-called closure problem a new set of equations has to be introduced. Those are the turbulence closure models, of which various approaches exist. To keep the structure compact, just the one being applied is explained further.

3.3.4 Classification of turbulence closure models

Following Laurien and Oertel (2018) turbulence models can generally be grouped in four categories as summarized in Table 3.1.

Table 3.1: Classification of turbulence models [Laurien and Oertel (2018)]

Class: / Category:	isotropic eddy viscosity	anisotropic Reynolds-tension
Algebraic models Models without transport Zero-equation models	Prandtl-mixing length Baldwin Lomax Model	algebraic Reynolds-tension models
Differential-equation models Transport models One/two-equation models	$k-\epsilon$ model $k-\omega$ model SST -model	$\tau-\epsilon$ model $\tau-\omega$-model

Reynolds tension models are used to model certain properties of flow connected to anisotropy of the turbulence, that can not be modelled by other turbulence models, for example secondary flow. They play no role in the framework of this thesis and are therefore not explained further.

A widespread concept underlying all the models in the left column of the table is to model the turbulence induced tension as an eddy viscosity. This viscosity induces an energy consumption during flow, analogously to the dynamic viscosity. However, it is not a material parameter but depends on the local flow properties. Due to the fact that the estimation of turbulence is reduced to one parameter in all three directions, isotropy of the turbulence is required. The Reynolds tensions are modelled as a single unknown viscosity depending on known averaged flow properties according to the Boussinesq-approximation (Laurien and Oertel (2018)):

$$\tau'_{ij} = \nu_t \left(\frac{\partial \bar{u}_i}{\partial x_j} + \frac{\partial \bar{u}_j}{\partial x_i} \right) - \frac{2}{3} k \delta_{ij}, \tag{3.10}$$

where δ_{ij} is defined as the Kronecker-delta.
As can be seen in Table 3.1 several approaches exist, to determine the parameter ν_t. The algebraic models in the top line rely on algebraic equations and are mostly used for very specialized applications due to their lack of accuracy on more general problems. An exception is the mixing length model of Prandtl, that is of major historical importance, and is still used especially for modelling the viscous underlayer of a flow, due to its high precision in this area proven by DNS (Laurien and Oertel (2018)).

3.3.5 Two-equation models

The most commonly used approaches in CFD are the two-equation models, introducing two additional transport equations for turbulent parameters. In REEF3D the models provided are the k-ϵ and the k-ω-model (Wilcox (2006)). Both models provide a transport equation for the specific turbulent energy k and a second transport equation for ϵ, respectively ω. An advantage of the k-ω-model is the resolution in vicinity to the wall. A third common approach is a mixture of both models, the SST-model (Menter (1993)), with a k-ω-model close to the wall and a k-ϵ one in distance to it. Since its application in this thesis, the main equations of the k-ω-model are introduced in the following.
ν_t is calculated taking into account the kinetic energy k, the specific turbulent dissipation ω (jr. Oertel et al. (2015)):

$$\nu_t = \frac{k}{\omega}. \tag{3.11}$$

The turbulent kinetic energy k is given by the fluctuating components of the velocity defined as:

$$k = \frac{1}{2}(u'^2 + v'^2 + w'^2) \tag{3.12}$$

Two additional transport equations are introduced to balance these two parameters.

$$\frac{\partial k}{\partial t} + u_j \frac{\partial k}{\partial x_j} = \frac{\partial}{\partial x_j}\left[\left(\nu + \frac{\nu_t}{\sigma_k}\right)\frac{\partial k}{\partial x_j}\right] + P_k - \beta_k k\omega \tag{3.13}$$

$$\frac{\partial \omega}{\partial t} + u_j \frac{\partial \omega}{\partial x_j} = \frac{\partial}{\partial x_j}\left[\left(\nu + \frac{\nu_t}{\sigma_\omega}\right)\frac{\partial \omega}{\partial x_j}\right] + \frac{\omega}{k}\alpha P_k - \beta\omega^2 \tag{3.14}$$

where P_k is the turbulent production rate and the coefficients have the empirically determined values $\alpha = \frac{5}{9}$, $\beta_k = \frac{9}{100}$, $\beta\frac{3}{40}$, $\sigma_k = 2$ and $\sigma_\omega = 2$ (Bihs (2018)) .

3.4 Computational methods

3.4.1 General methods

So far the mathematical formulas and models to describe the processes in a fluid within a given range of applications were described. For the implementation of these formulas in a CFD-solver, discretization from the continuum to a finite number of calculating points is required since the equations can not be solved analytically.
Three methods of discretization are typically applied in CFD. Of course each method has some typical advantages and disadvantages. These are (Ferziger and Perić (2008)):

Finite Volume Method The solution domain is split into a finite number of control volumes. The integrated form of the conservation equation is used to compute the exchange over the surface of the control element, with the values on the surface being interpolated from the variables known at the center of each volume. This results in an algebraic equation for each control volume, that includes variables from the computing node and the ones from the neighbouring cells. The main advantages are that the method is applicable to unstructured grids, conservatism is ensured and all the terms are physically interpretable. On the other hand higher orders than the second are difficult to obtain on unstructured grids.

Finite Elements Method The solution domain gets divided into a number of unstructured finite elements. The equations are multiplied with a weighting function before integrating them over the whole solution domain. The use of unstructured grids makes it possible to specifically refine it in areas of interest and adapt it to a wide number of geometries. The main difficulty is then the efficient solution method for the unstructured matrices.

Finite Differences Method The conservation equations are approximated for each point on a grid covering the solution domain by replacing the partial deriva-

tions using a discrete formulation based on the node values. This results in an equation for each grid point, that includes its own variables as well as a number of the neighbouring ones, depending on the order of the method. The main drawback is that a structured grid is required, which results in a comparatively high number of grid points. On the other hand the approach allows for higher order methods, and with progressing availability of computational resources the number of mesh points is of decreasing importance. This is the approach used in REEF3D.

3.4.2 Requirements

To make reliable calculations possible, a numerical tool has to fulfil a number of criteria. Since they are used to explain the advantages of several parts of the solver, a quick overview of them according to Ferziger and Perić (2008) is given before dealing with the details of the tool.

Consistency: With decreasing size of the mesh's cells the difference between the discretized solution and the exact one should converge to zero. It is usually estimated using Taylor-series.

Stability: The numerical method is called stable if the errors occurring during the calculation do not build up. For iterations that means, the solutions to it are not diverging. Examining this is difficult, especially for complex, non-linear equations. Many methods require the time step, not to exceed a certain level, so a criterion is introduced in subsection 3.4.3.

Convergence: Convergence describes the convergence to the exact solution of the differential equation. It is often demonstrated in showing that the method is stable and consistent.

Accuracy: Resulting from the fact that numerical solutions to flow problems are just approximations, several errors are induced. There are different types of errors that should be differentiated, to allow for precisely improve the numerical solution. These are:

Model errors: Deviation between the mathematical description of the problem and the real flow.

Discretization errors: Deviation of the exact solution of the differential equations and the discretized one.

Iterative errors: Deviation between the exact solution of the algebraic equation system and the iterative solution to it.

3.4.3 Finite differences method

Due to the application in this work, the main idea of the spatial discretization in the finite differences method is given in some more detail. For other general aspects of the discretization see the literature (for example Ferziger and Perić (2008), Griebel et al. (1998)).
Underlying to the method is a structured grid, which means an obvious relation to the neighbouring cells exists. The values of the variables at the knots, the intersections between the lines, are unknown. As mentioned above the idea of the method now consists of solving the local differential equation by approximating it by the tangent in use of the neighbouring values. A visualization for a one-dimensional discretization and three simple schemes can be seen in Figure 3.3.
The tangent is either formed by the right-neighbouring point (forward difference):

$$\left[\frac{du}{dx}\right] = \frac{u(x_{i+1}) - u(x_i)}{\Delta x} \tag{3.15}$$

the left neighbouring knot (backward difference):

$$\left[\frac{du}{dx}\right] = \frac{u(x_i) - u(x_{i-1})}{\Delta x} \tag{3.16}$$

or including both points(central differences):

$$\left[\frac{du}{dx}\right] = \frac{u(x_{i+1}) - u(x_{i-1})}{2 \cdot \Delta x} \tag{3.17}$$

From this simple example it can already be seen, how close the approximation gets to the precise solution, depending on the distance of the points and the method applied. The difference is decreasing with the number of knots included in the scheme for approximation. This can be shown by calculating the difference between Taylor-polynomials approximating the derivative and the approximations given above. An error dependent on the power of Δx is left. This exponent is referred to as the order of the discretization method, and describes how the error gets smaller with decreasing mesh size. For the presented approximations that means the central differences method is of second order, while the other methods are only of first order, so the error linearly depends on the grid size.
A problem for higher order discretization schemes can be non-physical oscillations affecting the stability of the solution (see subsection 3.4.2). They arise if the mesh discretization is too coarse (Griebel et al. (1998)). An illustration of this is given in Figure 3.4.
Resulting from this numerous schemes have been developed on approximating the

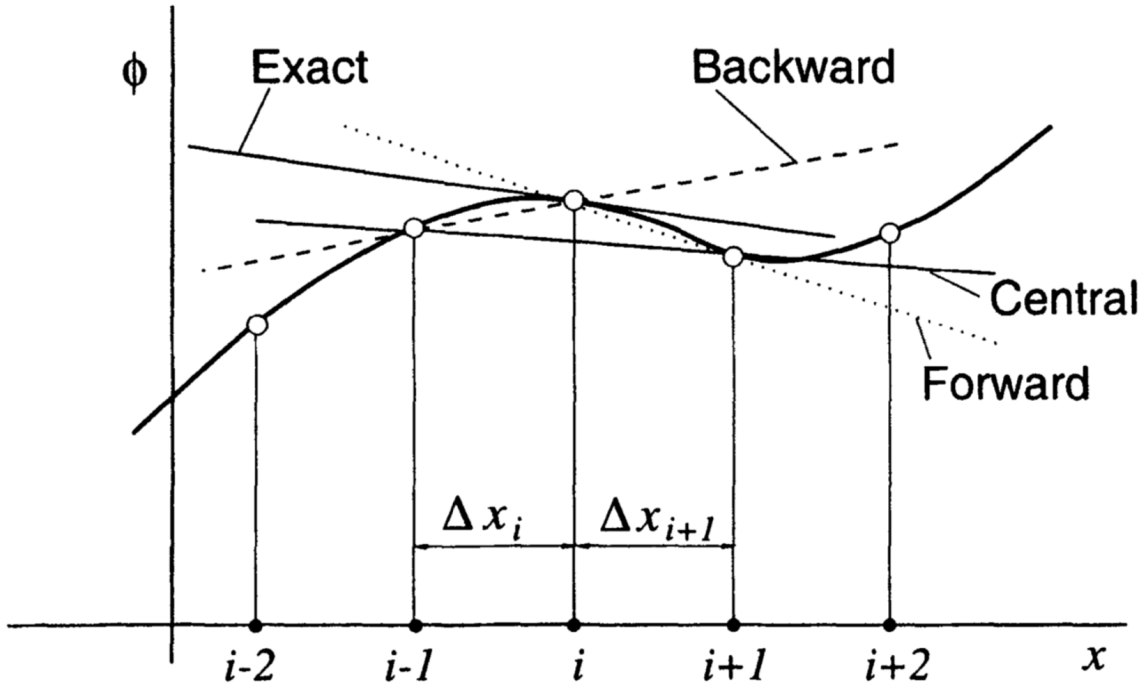

Figure 3.3: The different spatial discretization on a generic example for 1D [jr. Oertel et al. (2015)]
F

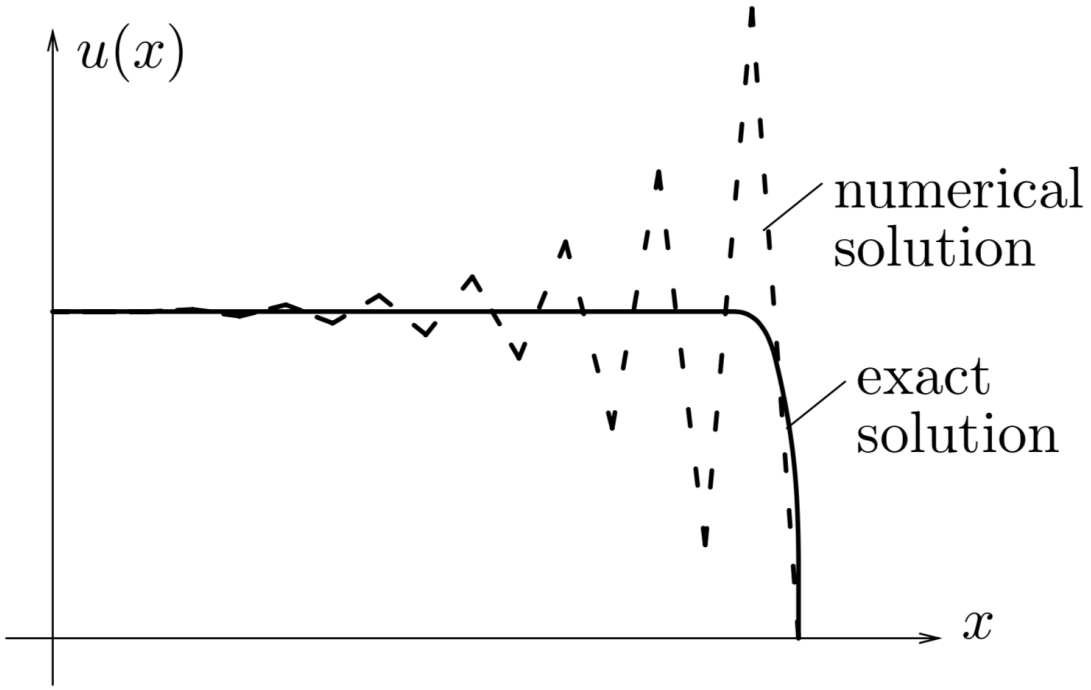

Figure 3.4: Illustration of stability problems on a diffusion/convection problem [Griebel et al. (1998)]

derivative. The scheme applied in the solver is presented in subsection 3.5.2.
The diffusive terms include the second order derivative, which means that the approximating schemes for the first derivative are just applied two times. For a central difference formulation this yields:

$$\left[\frac{d^2u}{dx^2}\right] = \frac{u(x_{i+1}) + u(x_{i-1}) - 2u_{x_i}}{\Delta x^2} \tag{3.18}$$

The time can be seen as a fourth coordinate direction, which is also discretized in time steps Δt. Different from the spatial coordinate the information is just transported in one direction. Any influence can only affect the future of the flow, there is no influence acting backwards (Ferziger and Perić (2008)). Consequently the discretization methods are adapted. A rather intuitive approach to it are the two level solution methods. For the generic variable Φ the value of a time step in the future can be determined adding the integral over the derivation in time, and then using the obtained value as a new initial value:

$$\Phi^{n+1} = \Phi^n + \int_{t_n}^{t_{n+1}} \frac{\partial \Phi}{\partial t} dt. \tag{3.19}$$

Four rather simple approaches to solve the discretized form of the integrals, that can

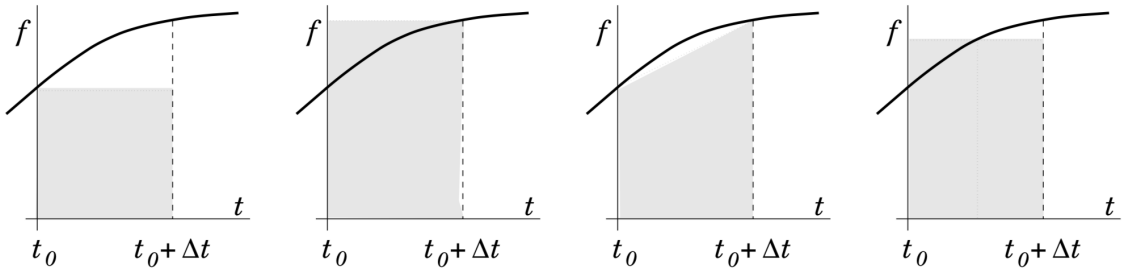

Figure 3.5: The four schemes for time discretization presented, from left to right: Explicit Euler, Implicit Euler, trapezoidal rule, midpoint rule [Ferziger and Perić (2008)]

still be geometrically interpreted (Figure 3.5) are given by Ferziger and Perić (2008). With $\frac{\partial \Phi}{\partial t} = f(t, \Phi(t))$ these are:

- The explicit Euler method uses the initial point $\Phi^{n+1} = \Phi^n + f(t_n, \Phi^n)\Delta t$
- The implicit Euler method uses the final point $\Phi^{n+1} = \Phi^n + f(t_{n+1}, \Phi^{n+1})\Delta t$
- The trapezoidal rule uses an interpolation between the points $\Phi^{n+1} = \Phi^n + \frac{1}{2}[f(t_n, \Phi^n) + f(t_{n+1}, \Phi^{n+1})]\Delta t$
- The midpoint rule uses the value in between the initial and final point $\Phi^{n+1} = \Phi^n + f(t_{n+\frac{1}{2}}, \Phi^{n+\frac{1}{2}})\Delta t$

Since all methods, except the explicit Euler method, require the unknown value of a time step t_n in the future, they require further approximations or iterations.
Like in space a number of more complex approximation of this derivative have been developed. The ones applied here are given in subsection 3.5.3. To ensure the stability of the methods, it has to be ensured, that the time step is sufficiently small. The Courant-Friedrich-Levy (CFL)-condition, as a method to set the timestep in reference to the spatial coordinate, is applied. It is defined as:

$$CFL = u\frac{\Delta x}{\Delta t} \leq 1. \tag{3.20}$$

The discretized expressions for both, time and space can then be written as a system of matrices, including initial and boundary-conditions, that is solved. Here again, various approaches exist. See for examples Ferziger and Perić (2008).

3.5 Implementation in REEF3D

3.5.1 Development of the model

REEF3D is a numerical tool developed at the department of civil engineering at the NTNU in Trondheim. It is designed under the premise of large super-computers available and focuses therefore on accuracy and the user productivity. The code is open source and written in C++, so that it is available for everyone and editable for many users due to the programming language being widely spread ((Bihs, 2018)). For post-processing the data paraview is suggested. After introducing the mathematical descriptions of the problem and giving a small overview over the basic concepts of solution methods in CFD, in the following the specific implementation in REEF3D is summarized.

3.5.2 Spatial discretization

Upon the different terms of the RANS equations, different methods of discretization are applied. The convective term typically suffers from numerical diffusion leading to a damping of waves. Another aspect is the stability and effectivity of the method. Higher order discretization schemes typically affect the numerical damping positively, while they are often problematic concerning stability. The WENO method according to Jiang and Shu (1996) is one that balances these needs. It is an extension of the ENO scheme adding extended limiters to improve the solution at discontinuous gradients.
By simply interpolating the values of the neighboured grid-knots the convection velocity $\tilde{u}$ is acquired:

$$u_i \frac{\partial u_i}{\partial x_i} \approx \frac{1}{\Delta x}(\tilde{u}_{i+1/2} u_{i+1/2} - \tilde{u}_{i-1/2} u_{i-1/2}) \tag{3.21}$$

Based on Equation 3.21 the WENO procedure then reads:

$$U^{\pm}_{i+1/2} = \omega^{\pm}_1 U^{1\pm}_{i+1/2} + \omega^{\pm}_2 U^{2\pm}_{i+1/2} + \omega^{\pm}_3 U^{3\pm}_{i+1/2} \tag{3.22}$$

This is the three ENO stencils $U^{1\pm}_{i+1/2}, U^{2\pm}_{i+1/2}, U^{3\pm}_{i+1/2}$, weighted with the use of the non-linear weights ω.
The three stencils are:

$$U^{1-}_{i+1/2} = \frac{1}{3}u_{i-2} - \frac{7}{6}u_{i-1} + \frac{11}{6}u_i$$

$$U^{2-}_{i+1/2} = -\frac{1}{6}u_{i-1} + \frac{5}{6}u_i + \frac{1}{3}u_{i+1} \tag{3.23}$$

$$U^{2-}_{i+1/2} = -\frac{1}{3}u_i + \frac{5}{6}u_{i+1} - \frac{1}{6}u_{i+2}$$

The inclusion of five points in total, make it a fifth-order scheme.
The weights are calculated as follows:

$$\omega_1^{\pm} = \frac{\alpha_1^{\pm}}{\alpha_1^{\pm} + \alpha_2^{\pm} + \alpha_3^{\pm}}, \quad \omega_1^{\pm} = \frac{\alpha_2^{\pm}}{\alpha_1^{\pm} + \alpha_2^{\pm} + \alpha_3^{\pm}}, \quad \omega_1^{\pm} = \frac{\alpha_3^{\pm}}{\alpha_1^{\pm} + \alpha_2^{\pm} + \alpha_3^{\pm}} \tag{3.24}$$

with:

$$\alpha_1^{\pm} = \frac{1}{10}\frac{1}{(\tilde{\epsilon} + IS_2^{\pm})^2}, \quad \alpha_2^{\pm} = \frac{6}{10}\frac{1}{(\tilde{\epsilon} + IS_2^{\pm})}, \quad \alpha_1^{\pm} = \frac{1}{10}\frac{1}{(\tilde{\epsilon} + IS_2^{\pm})}, \tag{3.25}$$

The weighting is done according to the smoothness of the function, and therefore the stability is increased. The weights will be largest for the stencil with the smoothest solution, while for stencils with larger gradients the weight will get smaller. For the case that two weights are put to zero, due to large gradients, the order will be three.

3.5.3 Time treatment

For the discretization in time high numerical accuracy and stability are required. The explicit third-order Total variation diminishing (TVD) Runge-Kutta scheme following Shu and Osher (1988) is fulfilling this requirements. The discretization is explicit and of third order. It is applied to the momentum equations and the level set function. For a generic variable ϕ, the equations are:

$$\begin{aligned}
\phi^{(1)} &= \phi^n + \Delta t L(\phi^n) \\
\phi^{(2)} &= \frac{3}{4}\phi^n + \frac{1}{4}\phi^{(1)} + \frac{1}{4}\Delta t L(\phi^{(1)}) \\
\phi^{n+1} &= \frac{1}{3}\phi^n + \frac{2}{3}\phi^{(2)} + \frac{2}{3}\Delta t L(\phi^{(2)})
\end{aligned} \tag{3.26}$$

To control the CFL number, adaptive time-stepping is applied, taking into account the influences from diffusion, velocity and a source term, such as gravity(Bihs et al. (2016):

$$\Delta t \leq 2\left(\left(\frac{|u|_{max}}{dx} + D\right) + \sqrt{\left(\frac{|u|_{max}}{dx} + D\right)^2 + \frac{4|S_{max}|}{dx}}\right)^{-1} \tag{3.27}$$

with the diffusion term:

$$D = max(\nu + \nu_t) \cdot \left(\frac{2}{(dx)^2} + \frac{2}{(dy)^2} + \frac{2}{(dz)^2} \right) \tag{3.28}$$

The discretization of the two-equation turbulence model, using an explicit time-stepping scheme such as TVD Runge-Kutta, would lead to a small time step compared to the one from the momentum equation. As a consequence, these equations are discretized with the use of an implicit first-order Euler scheme (Bihs et al. (2016)).
To solve the equations of the floating body, a second-order accurate Adams-Bashforth scheme is applied. For a generic variable ϕ, that is (Bihs and Kamath (2017)):

$$\phi^{(n+1)} = \phi^{(n)} + \frac{\Delta t}{2} \cdot (3\dot{\phi}^{(n+1)} - \dot{\phi}^{(n)}) \tag{3.29}$$

3.5.4 Pressure discretization

Unlike the other components of the RANS equations, there is no independent equation to calculate the pressure term. Chorin's projection method is applied in order to overcome this (Chorin (1968)).
In the predicter step, the pressure term is removed from the momentum equations. The resulting velocity after applying the time discretization is used to form a Poisson equation, the pressure needs to fulfil in order to ensure a divergence free flow field (Bihs et al. (2016)):

$$\frac{\partial}{\partial x_i} \left(\frac{1}{\rho(\phi^n)} \frac{\partial p^{n+1}}{\partial x_i} \right) = \frac{1}{\Delta t} \frac{\partial symustern}{\partial x_i} \tag{3.30}$$

The solution of this equation is obtained using the BiCGStab algorithm from the HYPRE library (van der Vorst (1992)). This iterative method is applied due to high computational expenses it takes to solve the equation. In the next time step, the divergence free velocity is acquired by correcting the intermediate velocity field with the resulting pressure term:

$$u_i^{n+1} = u_i^* - \frac{\Delta t}{\rho(\phi)} \frac{\partial p}{\partial x_i} \tag{3.31}$$

3.5.5 Turbulence model in REEF3D

As mentioned in subsection 3.3.5, a k-ωmodel is applied. In addition to the general approach, REEF3D includes some additional terms which are explained in the following (Bihs et al. (2016)).
To include the surface roughness, Schlichting's rough wall formulation is used at solid boundaries (Schlichting (1979)) :

$$u^+ = \frac{1}{\kappa} ln \left(\frac{30y}{k_s} \right). \tag{3.32}$$

To avoid overproduction, an eddy viscosity limiter for the region outside of the boundary layer is established. As a consequence, two terms for the calculation of ν_t are evaluated according to:

$$\nu_t = min \left(\frac{k}{\omega}, \sqrt{\frac{2}{3}} \frac{k}{|S|} \right) \tag{3.33}$$

In the region of the free surface the dissipation is increased: Since this is usually not included within turbulence model and would lead to an overestimation of the turbulence close to the surface, a damping-scheme is included.
This is:

$$\omega_s = \frac{c_\mu^{\frac{1}{4}}}{\kappa} k^{\frac{1}{2}} \cdot \left(\frac{1}{y'} + \frac{1}{y_*} \right) \tag{3.34}$$

,with $y' = 0.07$ $c_\mu = 0.07$ and $\kappa = 0.4$ (Bihs et al. (2016)).

3.5.6 Free surface capturing

To account for the free surface in the intersection between water and air, the flow is modelled as a two-phase system. The level set function ϕ describes the shortest distance to the interface Γ. The interface is defined as the zero contour, while the two phases are distinguished by the change of the sign (Osher and Sethian (1988)):

$$\phi(\vec{x}, t) \begin{cases} > 0 & if \quad \vec{x} \in phase1 \\ = 0 & if \quad \vec{x} \in \Gamma \\ < 0 & if \quad \vec{x} \in phase2 \end{cases} \tag{3.35}$$

A convection equation is introduced for the level set function. This is:

$$\frac{\partial \phi}{\partial t} + u_j \frac{\partial \phi}{\partial x_j} = 0 \tag{3.36}$$

This equation is solved numerically with use of the Hamilton-Jacobi version of the WENO scheme in space and the third order TVD Runge-Kutta scheme in time. In order to keep the signed distance property of this function, that would otherwise be lost with evolvement of the interface, a reinitialization algorithm is included that reads (Sussman et al. (1994)):

$$\frac{\phi}{\partial t} + S(\Phi) \left(\left| \frac{\partial \phi}{\partial x_j} \right| - 1 \right) = 0. \tag{3.37}$$

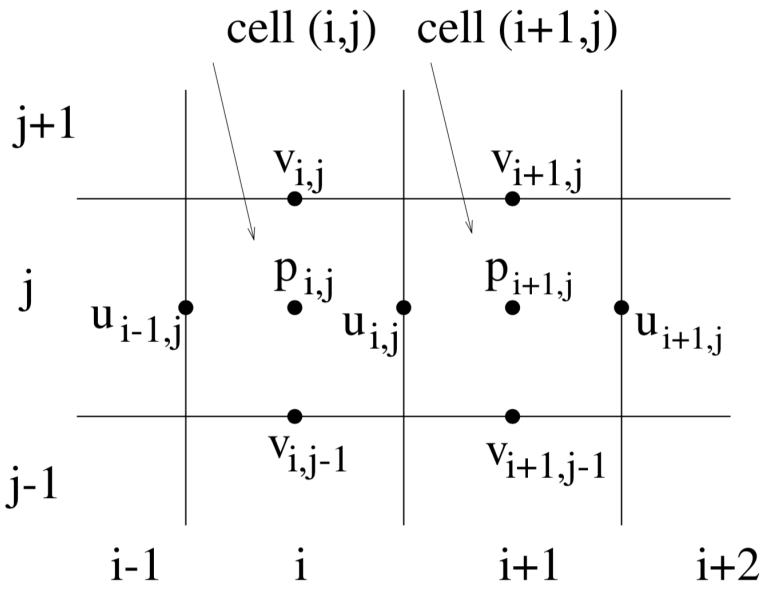

Figure 3.6: A staggered grid [Griebel et al. (1998)]

3.5.7 Immersed boundary

The grid applied is a staggered one, meaning that in contrast to a collocated one the variables are not all defined on the knots but on different points within the grid (Figure 3.6). This is favourable especially regarding the pressure-velocity coupling. The boundaries are defined as ghost cell immersed boundaries in all three dimensions (Berthelsen and Faltinsen (2008)). That is an extrapolation to fictious ghost cells lying in the solid region. Hence the solver does not have to account for the conditions explicitly, but they are enforced implicitly. Complex geometries to the grid can be included via the STL-format, that can be generated from CAD-files. Simpler geometries such as boxes, cylinders and wedges can be included directly.

3.5.8 Parallelization

REEF3D relies on supercomputer capacities for being able to provide high accuracy on a small scale. To do so, advanced parallelization strategies are the key to make use of the capacities effectively. The strategy used is the domain decomposition (Bihs et al. (2016)). The simulation domain is split into several smaller domains which are exchanging information on their boundaries through ghost cells. Making use of the same method as for the solid boundary has the advantage of straight-forward coding. For the exchange of the ghost cell values, the Message passing interface (MPI) is used. Due to the use of the fifth order discretization scheme, three layers of ghost cells are

necessary.

3.5.9 Numerical wave tank

A numerical wave tank is implemented in REEF3D. It consists of a cuboid with boundary conditions on each of the six sides. It is split into three sections, a wave generation zone, a middle zone where the experimental set-up is placed and an absorption zone to prevent any reflections from the end of the tank (Bihs et al. (2016)). For illustrative purposes see Figure 4.1.
The waves are generated and absorbed using the wave relaxation method. In comparison to a Dirichlet type boundary, this leads to waves of higher quality (Mayer et al. (1998)). Within the generation zone, the wave parameters are smoothly ramped up to the analytical values of the wave theory chosen, while they are smoothly transformed to the parameters of the still water level within the absorption zone. With the dimensionless parameter $\tilde{x}$ for the length of the relaxation zone this reads:

$$u(\tilde{x})_{relaxed} = \Gamma(\tilde{x})u_{analytical} + (1 - \Gamma(\tilde{x}))u_{computational} \tag{3.38}$$

$$w(\tilde{x})_{relaxed} = \Gamma(\tilde{x})w_{analytical} + (1 - \Gamma(\tilde{x}))w_{computational} \tag{3.39}$$

$$p(\tilde{x})_{relaxed} = \Gamma(\tilde{x})p_{analytical} + (1 - \Gamma(\tilde{x}))p_{computational} \tag{3.40}$$

$$\phi(\tilde{x})_{relaxed} = \Gamma(\tilde{x})\phi_{analytical} + (1 - \Gamma(\tilde{x}))\phi_{computational} \tag{3.41}$$

Γ is the relaxation function (Jacobsen et al. (2012)):

$$\Gamma(\tilde{x}) = 1 - \frac{e^{\tilde{x}^{3.5}} - 1}{e - 1} \tag{3.42}$$

The analytical parameters are defined according to the wave theory chosen by the user, such as linear waves, 2nd-order Stokes theory or 5th-order Stokes theory.

3.5.10 Floating algorithm

To describe the geometry of the solid body, a surface mesh is implemented. This can be done by most CAD-programs exporting STL data files, or by using an internal algorithm of the tool for simple geometries. The intersections to the underlying Cartesian grid are determined with a ray-tracing algorithm, that calculates the shortest distance from a grid point to the closest triangle (Yang and Stern (2013)).

A reinitialization algorithm according to Sussman et al. (1994) is again applied, returning signed distance properties for a level set function in the vicinity of the solid body. The ghost cell immersed boundary method of Berthelsen and Faltinsen (2008) is applied to treat the solid fluid interface .
Using the pressure and viscous stress tensor, the forces acting on the surface Ω can be determined as (Bihs and Kamath (2017)):

$$F_{i,e} = \int_{\Omega} (-n_i p + n_i \tau) d\Omega. \tag{3.43}$$

The acting moments on the body result as (Bihs and Kamath (2017)):

$$M_{i,e} = \int_{\Omega} R \times (-n_i p + n_i \tau) d\Omega, \tag{3.44}$$

with the distance to the center of gravity R and the surface of the body Ω.
Any point of the rigid structure is described by the body's center of gravity and the orientation in the inertial coordinate system. Using Euler angles to describe the position leads to the position vector (Bihs and Kamath (2017)):

$$x = (x_1, x_2, x_3, x_4, x_5, x_6)^T \tag{3.45}$$

with the first components being the coordinates of the center of gravity, and the last three ones being the three Euler-Angles ϕ, θ and ψ.
The introduction of a separate coordinate system for the solid body simplifies the calculation of the body's movement. The fluid flow is calculated in an inertial coordinate system, and the floating body in a non-inertial coordinate system, so that the the forces and moments can be calculated in the inertial system. The rotation components in the non-inertial coordinate system are then given with:

$$\xi = (\xi_1, \xi_2, \xi_3)^T \tag{3.46}$$

With the origin of the non-inertial coordinate system positioned in the body's center of gravity the moments of inertia are (Bihs and Kamath (2017)):

$$I = \begin{bmatrix} I_x & 0 & 0 \\ 0 & I_y & 0 \\ 0 & 0 & I_z \end{bmatrix} = \begin{bmatrix} mR_x^2 & 0 & 0 \\ 0 & mR_y^2 & 0 \\ 0 & 0 & mR_z^2 \end{bmatrix} \tag{3.47}$$

with m the mass of the body and R_x, R_y and R_z the distances of a point to the center of gravity. To transfer the acting moments M on the system from the flow to the non-inertial system, it is necessary to include a rotational matrix.

$$\boldsymbol{M_\xi} = (M_{1,\xi}, M_{2,\xi}, M_{3,\xi})^T = \boldsymbol{J^{-1}} \cdot \boldsymbol{M_x} \tag{3.48}$$

This results in a description of the translational movements as:

$$\begin{pmatrix} \ddot{x_1} \\ \ddot{x_2} \\ \ddot{x_3} \end{pmatrix} = \frac{1}{m} \cdot \begin{pmatrix} F_{x_1,x} \\ F_{x_2,x} \\ F_{x_3,x} \end{pmatrix} \tag{3.49}$$

where F_x are the acting forces upon the system (Martin et al. (2018*a*)). The rotational movements are described with the Euler equations in the non-inertial system (Fossen (1994)).

$$\begin{aligned} I_x\ddot{\xi_1} + \dot{\xi_2}\dot{\xi_3} \cdot (I_z - I_y) &= M_{1,\xi} \\ I_y\ddot{\xi_2} + \dot{\xi_1}\dot{\xi_3} \cdot (I_x - I_z) &= M_{2,\xi} \\ I_z\ddot{\xi_3} + \dot{\xi_1}\dot{\xi_2} \cdot (I_y - I_x) &= M_{3,\xi} \end{aligned} \tag{3.50}$$

By integrating 3.49 twice, the position of the body can be calculated analytically, while the system 3.50 is solved numerically using the second-order accurate Adam-Bashforth scheme (see subsection 3.5.3).
For physical interpretation the Euler angles need to be transformed back into the inertial coordinate system.
Fluid-structure coupling is done in a a weak form. Acting forces from the fluid on the structure are calculated first, and the position of the structure is calculated. The fluid properties are updated afterwards, including the boundary-conditions of the solid in use of the ghost cell immersed boundary method (Berthelsen and Faltinsen (2008)). The velocities and pressure are both calculated from the motion of the body.

3.5.11 Mooring models

Catenary mooring model

Three different models to account for the behaviour of the mooring lines of different complexity can be applied within the framework of the tool. Due to the different scale in space of the mooring lines compared to the floating body, a direct inclusion via the RANS equations would require the model to be extremely high resolved. Regarding the inefficiency of this approach other ways of calculating the forces from the mooring lines upon the structure are presented.
The simplest approach is an analytical way, the so called catenary model. Here, the forces are just calculated dependent on the starting and end point of the line and its weight. To apply this model, parts of the mooring line have to lay on the ground. Static conditions with no current have to be assumed in order to find an analytical solution. A sketch of a line with the different parameters can be seen in Figure 3.7.

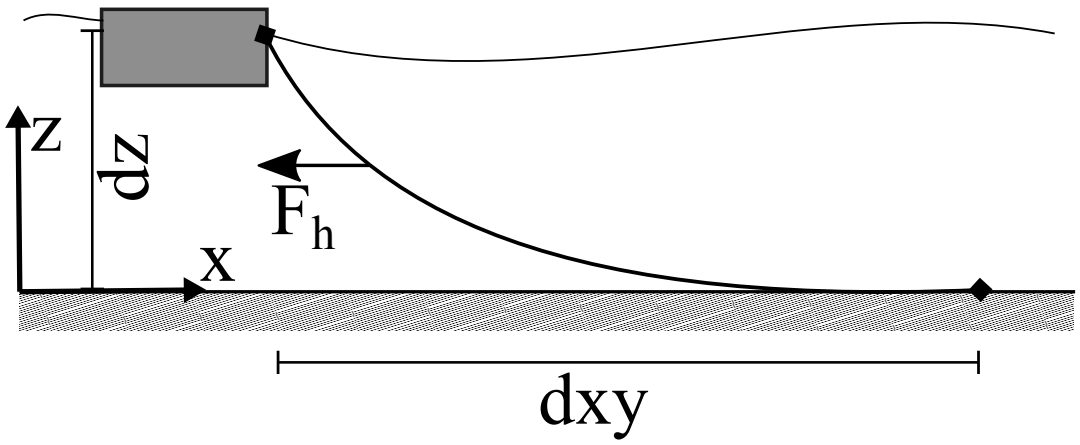

Figure 3.7: Catenary mooring model

A catenary equation describes the shape of a line dependent on the weight and external forces as follows (Faltinsen (1990)):

$$z(x,y) = \frac{F_h}{\gamma_0} \cdot \left(cosh\left(\frac{\gamma_0}{F_h} \cdot \sqrt{x^2+y^2} \right) \right) \tag{3.51}$$

The influence of the mooring system on the body is included in a weakly coupled form. Hence, the forces acting on the body by the mooring system need to be calculated. The tension forces F_T are calculated as follows:

$$F_T(z) = F_h + \gamma_0 dz + (z - dz) \cdot (\gamma_0 + \rho g A) \tag{3.52}$$

Dependent on the distance between the fixed anchor point and the time varying attachment point on the floating body, the horizontal force is calculated using a Newton-Raphson algorithm for the following equation:

$$dxy = \sqrt{dx^2 + dy^2} = L - dz \cdot \sqrt{1 + 2 \cdot \frac{F_h}{\gamma_0 dz}} + \frac{F_h}{\gamma_0} \cdot cosh^{-1}\left(1 + \frac{\gamma_0 dz}{F_h}\right) \tag{3.53}$$

Knowing this force, the forces at each mooring point are calculated as follows:

$$X = F_h cos\left(tan^{-1}\left(\frac{dx}{dy} \right) \right), \tag{3.54}$$

$$Y = F_h sin\left(tan^{-1}\left(\frac{dx}{dy} \right) \right), \tag{3.55}$$

$$Z = F_h dz \cdot \sqrt{1 + \frac{2F_h}{w dz}}. \tag{3.56}$$

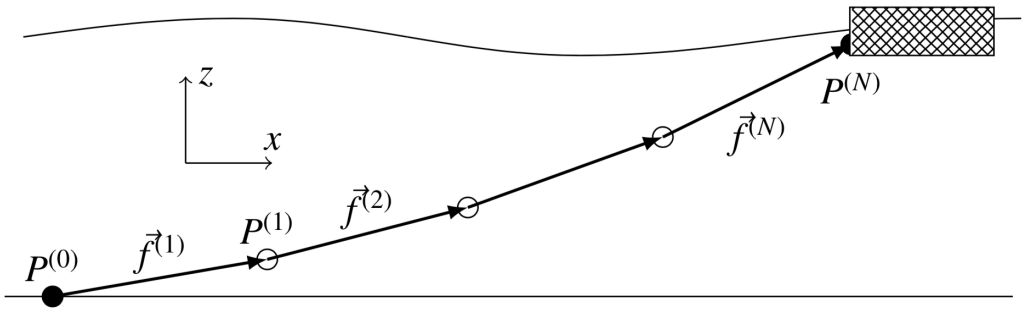

Figure 3.8: Discretization of the mooring lines [Martin et al. (2018*b*)]

The moments can then be computed multiplying the forces with the distances to the center of gravity.

Quasi-static model

A more sophisticated approach that balances the need for a more precise calculation and computational cost, is a quasi-static model, originally developed for floating nets. It is not restricted to lines that partly lay on the floor and therefore allows for a more general use. Details can be found in Martin et al. (2018*c*) and Martin et al. (2018*b*). The dynamic of a mooring line neglecting bending stiffness is represented by the following equation of motion:

$$\gamma_0 \ddot{r} = \frac{\partial}{\partial s}(F_T \vec{f}) + f_{ext}, \tag{3.57}$$

This equation is simplified assuming small line motion in time and steady state flow of the fluid:

$$\frac{\partial}{\partial s}(F_T \vec{f}) = -f_{ext}, \tag{3.58}$$

This force equilibrium is discretized splitting each line into N bars of length l with the knots P in between as can be seen in Figure 3.8 . Consequently the outer knots are connected to the floating body and the bottom.
Gravity forces are taken into account distributing the line's mass equally on all knots:

$$\vec{F_G^{(j)}} = \gamma_0 \cdot \vec{g} \cdot \frac{\rho_m - \rho}{\rho_m} \cdot \frac{l^{(j)} + l^{(j+1)}}{2}, j =, ...N - 1 \tag{3.59}$$

The hydrodynamic forces F_H are taken into account using Morison's formula at each bar:

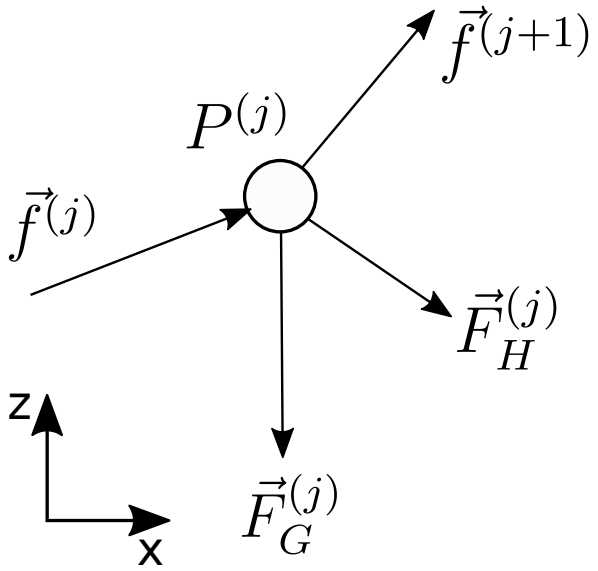

Figure 3.9: Force equilibrium on a single node $P^{(j)}$

$$\vec{F_H}^{(j)} = l^{(j)} d^{(j)} \frac{\rho}{2} \cdot [c_t(u_i \cdot \vec{f})]|u_i \cdot \vec{f}| \cdot \vec{f} + c_n(u_i - (u_i \cdot \vec{f}) \cdot \vec{f})|u_i - (u_i \cdot \vec{f}) \cdot \vec{f}|]^{(j)}, j = 1, ..., N \tag{3.60}$$

Finally this leads to the discrete formulation for the inner knots for the knot $P^{(j)}$, illustrated in Figure 3.9 :

$$\vec{f}^{(j+1)} F_T^{(j+1)} - \vec{f}^{(j)} F_T^{(j)} + \vec{F_H^{(j)}} + \vec{F_G^{(j)}} = \vec{0}, j = 1, ..., N-1 \tag{3.61}$$

The elasticity is included by calculating the length l dependent o the force F_T. Furthermore a geometrical constraint is added to ensure the same number of equation as unknown variables. This is the length of al bars adding up to the distance between the anchoring points $\vec{L}$:

$$\sum_{j=1}^{N} \vec{f}^{j} l^{(j)} = \vec{L} \tag{3.62}$$

This leads to a system of equation that is solved using an iterative method following Hackmann (1983). Dynamic transparency is assumed, so that no influence from the mooring model on the fluid is taken into account. Only the resulting forces and directions on the floating body originating are included on the Fluid structure interaction (FSI) solver, adding the forces to the fluid forces.

Chapter 4

Validation of the floating algorithm

4.1 Set-up

To allocate possible errors the numerical models got stepwise more complex, starting with an empty wave tank, then adding the barge first in decay-tests, afterwards under regular waves and finally ending up with the moored floating body under wave load. Due to the computational expenses, it was chosen to perform the simulations in two dimensions. The numerical wave tank of REEF3D was used as described in subsection 3.5.9. The wave generation zones were chosen according to the wavelength of the tested wave λ, with one wavelength for the generating zone and twice the wavelength for the damping zone. An exception is the wave with a period of 1.6 s where only one wavelength for damping was used due to the large extension. The barge was placed in the middle of the tank in its main direction. A sketch of this set-up can be seen in Figure 4.1.
In the solver, 2D simulations are designed in a way that one slice of the real world set-up is modelled consisting of only one layer of cells. This means the width of the model depends on the cell size of the mesh. The barge was implemented in a manner,

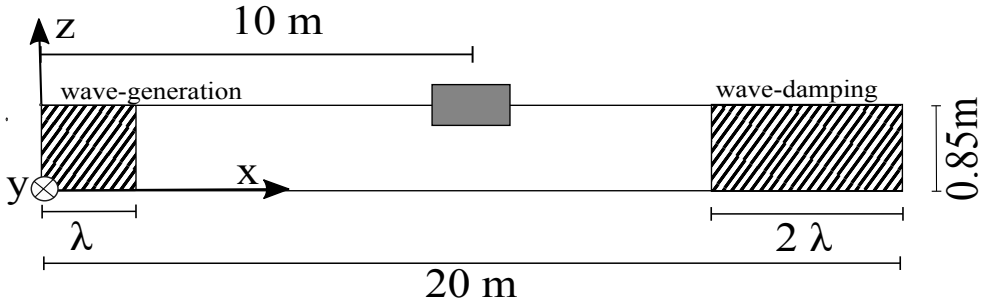

Figure 4.1: Sketch of the barge in the numerical wave tank

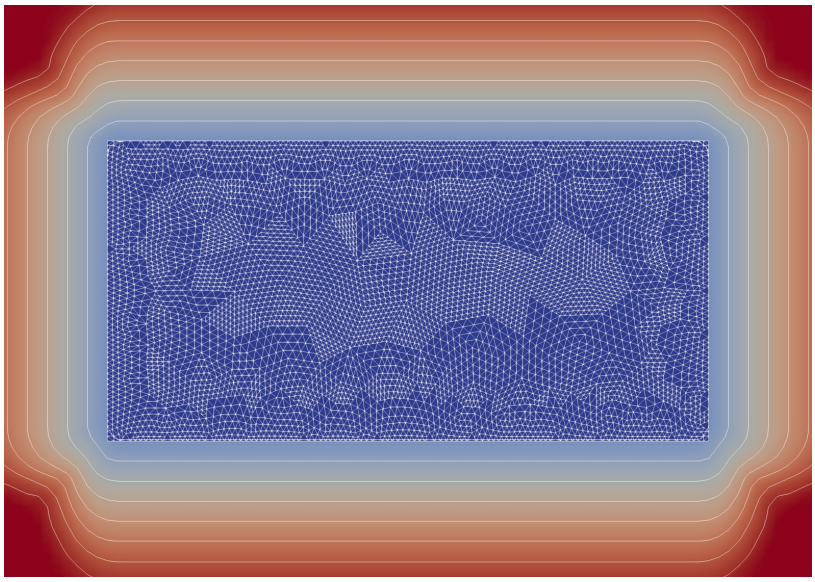

Figure 4.2: Contour of the level set function describing the boundary to the solid body ($\Delta x = 0.005m$)

that it had the same width. Its initial position was chosen in respect to the floating equilibrium, meaning that the initial center of gravity was located at z = 0.823 m and no initial angle was assumed. The contours of the level set function describing the boundary of the barge can be seen in Figure 4.2
Considering the fact, that in a 2D model the wave gauge can not be positioned next to the barge, it was moved 2 m in front of its location. Consequently the heave motion does not match with the surface elevation, but general comparisons of the values or effects on the wave height are still possible.

4.2 Parameter study

4.2.1 Wave theory

A first step to reproduce the experimental tests was to choose the appropriate wave theory. Therefore, waves with a period of 0.8 s were generated with different approaches in a numerical wave tank without any structure inside and compared with elevation measurements of the empty physical flume. The wave period was chosen as it is known that differences might get more obvious on steeper waves. The wave theories applied were linear waves for intermediate water depth, 2nd order stokes waves and 5th order Stokes waves. The results can be seen in Figure 4.3.
No influence of the theory on the elevation can be seen, so that 2nd order Stokes

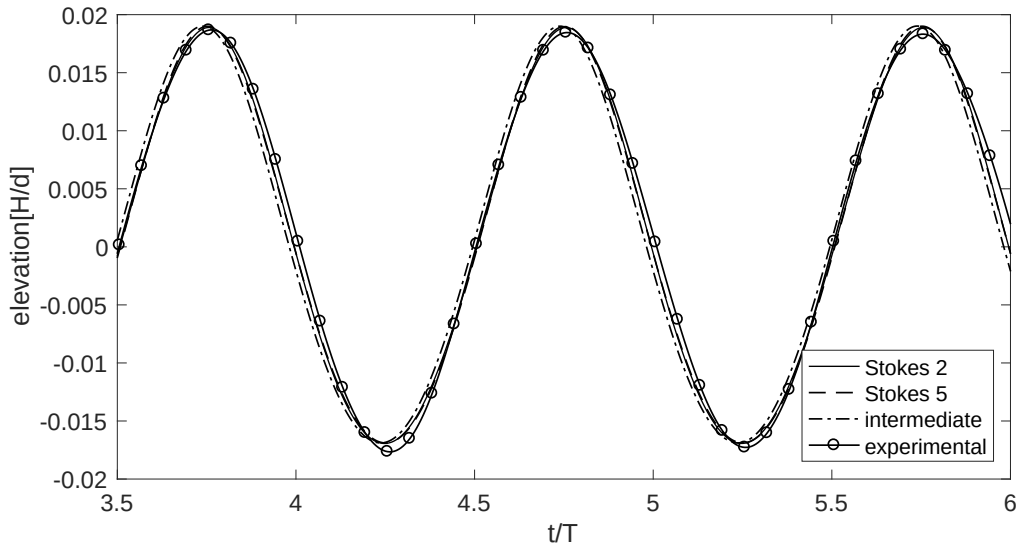

Figure 4.3: Three different wave theories and experimental test compared in an empty tank, T=0.8 H=3cm

theory was chosen for all further numerical set-ups conducted. The experimental and numerical datasets match very well.

4.2.2 Tank Length

A second important parameter is the appropriate length of the tank. The shorter the tank is, the less cells have to be modelled. Hence, the computational costs reduce drastically. On the other hand there is a risk of reflecting waves influencing the movement of the body, even though the numerical damping implemented is quite effective. To exclude this potential error source, two different tank lengths were compared. One with a length of 12m, the other one with a length of 20m. If the results would match, the shorter one was chosen, otherwise the computationally more expensive longer one had to be used. In Figure 4.4 the results for the decay-tests can be seen, in Figure 4.5 the results for a regular wave are visible.
As can be seen, the tank length has no influence in the beginning of the heave decay test, but after some seconds there are reflections inducing additional movements in the shorter tank, while on the longer tank a still status is reached. For the pitch decay test, an influence can be seen during almost the entire test, with significantly higher amplitudes of the movement in the shorter wave tank.
The tank length also has an influence on the movement in regular waves. For waves with a period of 1.6s the heave amplitude is smaller in the shorter tank, while the pitch amplitude is higher. As a consequence, the longer tank with a length of 20m is

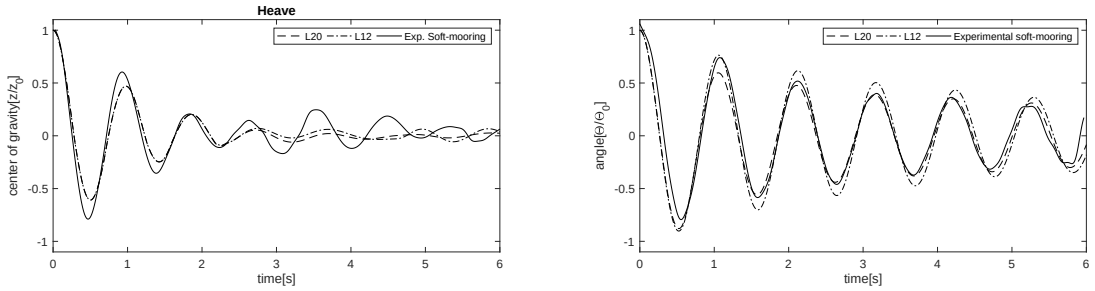

(a) (b)

Figure 4.4: Decay-test for two different tank lengths compared to the experimental data

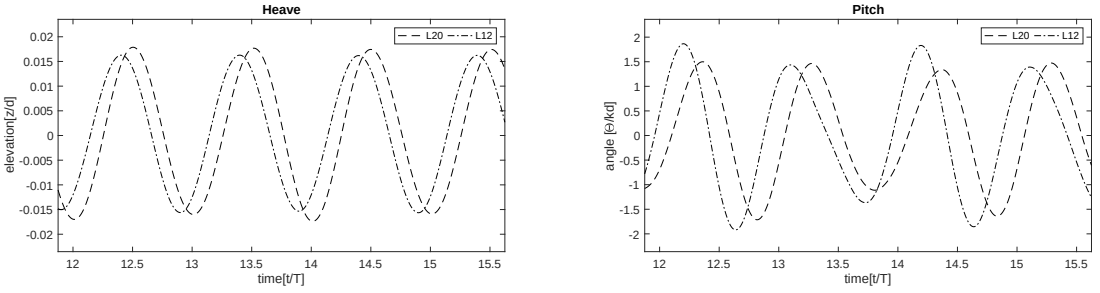

(a) (b)

Figure 4.5: Regular waves for two different tank lengths (T = 1.6s, H = 3cm)

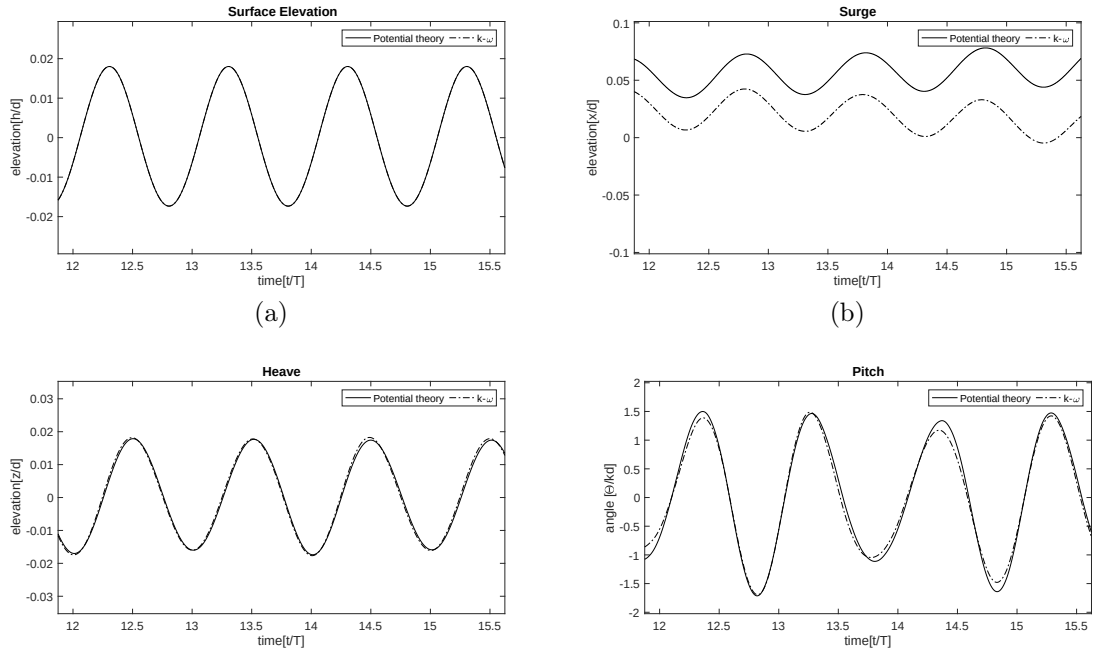

Figure 4.6: Comparison of the $k-\omega$-turbulence model with the potential solution (T = 1.6 s, H = 3 cm)

used in all following models.

4.2.3 Turbulence-model

Instead of modelling the turbulence, it is also possible to just set the turbulent viscosity to 0. That means energy consumption is not taken into account, but the results equal the ones from applying the potential theory. Since the goal of developing the CFD solver is to overcome the limitations of this approach, it is clearly desired to take a turbulence model into account. Since the parameters of the validation data generated are similar to ideal conditions for applying the potential theory both results are compared, to see if the deviations are as small as expected.
In Figure 4.6 the movements under waves with a period of 1.6s can be seen for models with potential theory and k-ω turbulence-closure. The amplitude of the pitch motion is reduced in some points with the application of the pitch motion. The heave motion is almost unaffected. Furthermore it can be seen, that the drift motion is reduced with the use of the turbulence model. The differences between the two variants are considered negligible, so that the k-ω model is applied.

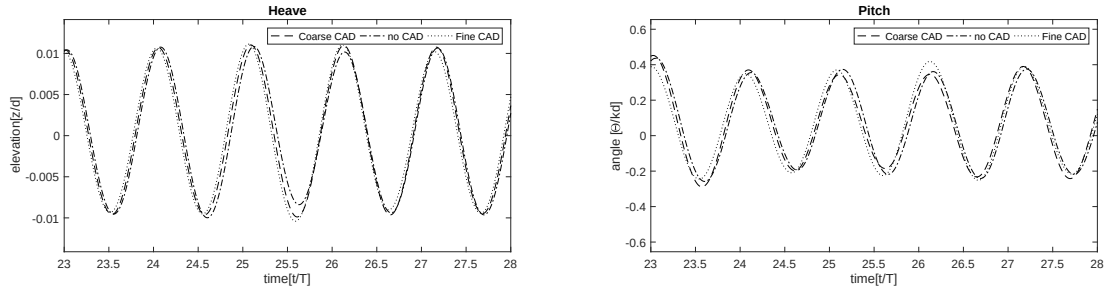

(a) (b)

Figure 4.7: Comparison of the movement in regular waves for three different meshes for the floating body ($\Delta x = 0.005m$ T=0.8s H=3cm)

4.2.4 Mesh of the floating body

The tool provides the possibility to include floating bodies, via generating its mesh in a CAD tool. This is the only possibility to influence the resolution of the mesh. Three different models for the floating body's grid have been compared for a body under regular waves with T = 0.8 s and H = 3 cm. The wave was chosen, due to the rapid movement of the barge and the following sensitivity. The resulting movements are shown in Figure 4.7. The three meshes are a coarse one generated in a CAD-tool, one using REEF3D's internal meshing algorithm and a higher resolved mesh generated with CAD. The advantage of a CAD-tool is, that the mesh can be designed with a higher resolution on critical points, such as edges. Therefore the number of triangles is not the only parameter having an influence on the quality.
It can be seen that the influence of the body's grid is not to high, but at some points the predicted motion for both heave and pitch is lower, when the lower resolved meshes are applied. Hence, the finer mesh generated with the CAD-tool is used in all following models.

4.2.5 Springs

The soft-mooring system in the experimental test was included to prevent the model from drifting within the channel. The same effect can also be observed in the numerical models, especially in the shorter waves. This leads to a change in the period of the barge's movements, since the wave forces are attacking at a different time in other places. To prevent this from happening a set of springs is included exceeding a force on the floating body linearly increasing with the displacement, just the same as in the experimental tests. To include them in a two dimensional model, their stiffness constant needs to be adapted, by dividing them by the share one cell has of the body's width.

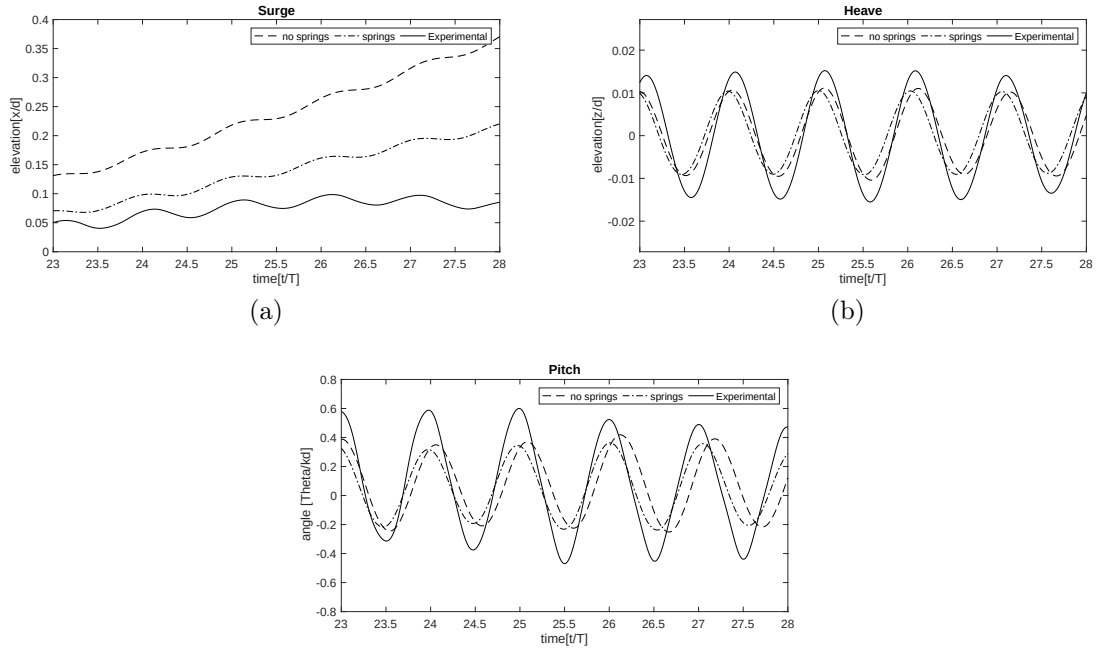

Figure 4.8: The movement of the body with and without springs ($\Delta x = 0.005m$, T= 0.8 s, H = 3 cm)

For waves with a period of 0.8 s (Figure 4.8), it can be seen that the drift motion is reduced significantly even though it is still quite high with the springs implemented. The springs almost have no influence on the heave amplitude of the body. The motion is slightly shifted, reaching the maxima earlier then without springs and showing some prolongation of the period due to the still existing drift. A similar influence can be observed for the pitch motion, the motion is shifted as well, and a small increase in the period can be seen. The amplitude is slightly higher, when no springs are taken into account.
The movement shown in Figure 4.9 for waves with a period of 1.2 s is also not drastically influenced by the springs. Without the springs the barge is drifting against the wave direction, with springs this is reduced, but still some drift can be observed. In the part examined the surge motion is constantly oscillating about the same value. The amplitude in heave direction is better reproduced without springs, but the difference in between the numerical models is not big. The difference to the experimental data is about one fourth. Induced by the surge movement a change of period can be observed, with the free-floating model having a reduced period, due to the drift motion. This can not be seen for the model including springs, following the prevention of further drift movements. In the pitch motion it can be seen, that the results are very similar in the beginning of the time series, but closer to the ending the am-

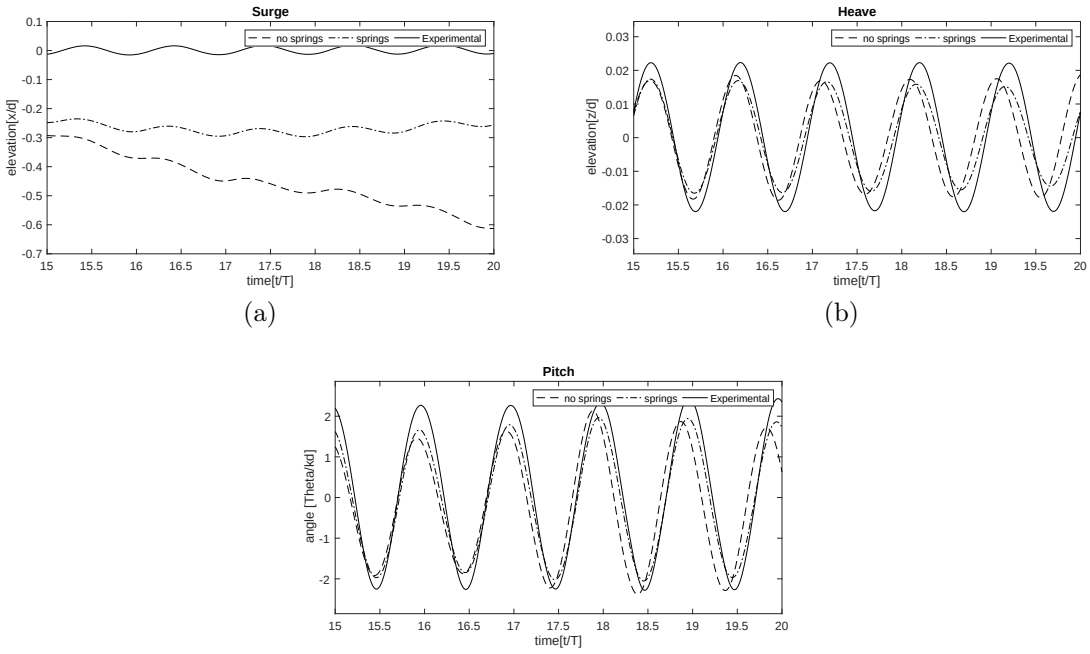

(a) (b) (c)

Figure 4.9: The movement of the body with and without springs ($\Delta x = 0.005m$, T= 1.2 s, H = 3 cm)

plitude without the springs increases, while it stays more constant, when springs are included.
For a period of 1.6 s (Figure 4.10) the numerical results show the best match to the experiments. The drift motion is only small, for both numerical cases. For the heave motion the springs do not seem to have any influence. The pitch motion shows some irregularities for both of the numerical models, especially in the lowest points. For the pitch motion some differences can be observed, the amplitude is reduced slightly by the application of the springs.

4.3 Convergence

4.3.1 Decay-tests

To evaluate an appropriate resolution for the mesh, the decay tests as well as the tests under regular waves were calculated on three different grids and compared afterwards. The cell sizes were 10mm, 7mm and 5mm.
In Figure 4.11 the decay tests for three different mesh resolutions can be seen, compared to the experimental tests performed. Since the initial displacement in the experimental test differ slightly, the movement is normalized with the initial displace-

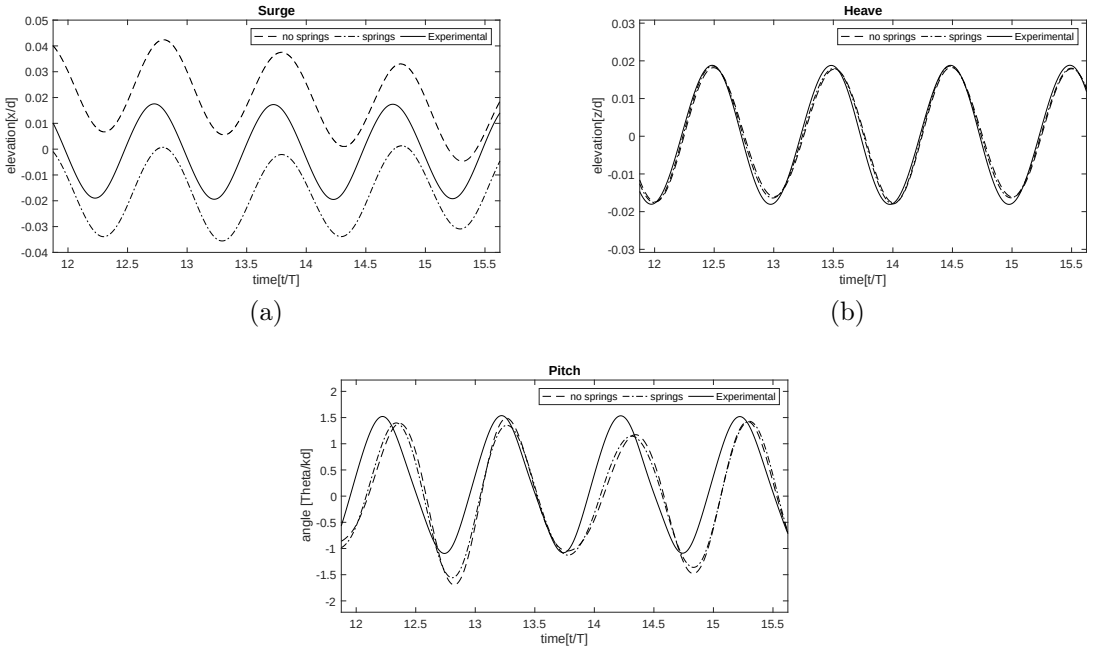

(a) (b)

(c)

Figure 4.10: The movement of the body with and without springs ($\Delta x = 0.005m$, T= 1.6 s, H = 3 cm)

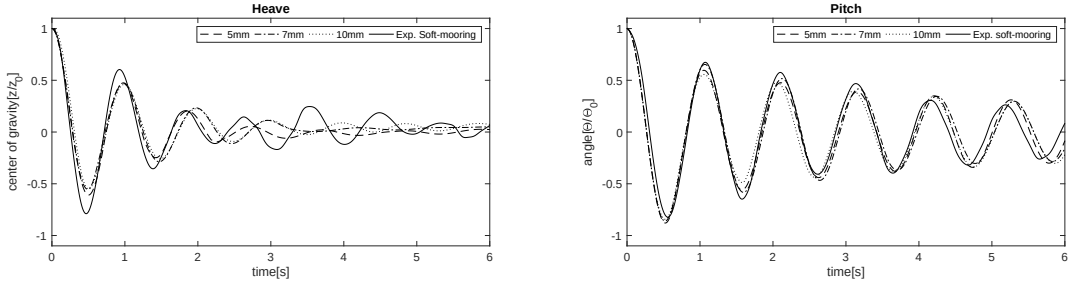

(a) (b)

Figure 4.11: Comparison of the decay-test for three mesh resolutions

ment, to allow for comparison with the decay tests for both the soft-mooring-system as well as free floating. As stated in Meyer (2018), the influence of the soft-mooring system is marginal, so that just the results for the soft-mooring system are given here for a more lucid presentation.
For the heave decay test, it can be stated that in general the three numerical models are damped too much in comparison to the experimental dataset. The length of the first two periods is well reproduced by the 5mm-model, while the other ones show a longer phase already in the second period. After that, none of the models matches the dataset, but it can also be seen, that in this part of the data series, show some unexpected behaviour. That is the peak at 3.5 s being higher than the one at 2.5 s, which is a sign of non-physical behaviour of the barge, so that the comparison should focus more on the beginning of the time series. Here, also the amplitude is reproduced better by the highly resolved grid than by the two other ones, but still the difference is about one fourth compared to the experimental dataset.
For the pitch decay-test the reproduction is in total better. All the models tested show a really small difference in the period compared to the experiments. The amplitude is also well reproduced, with differences between a fifth and a tenth.

4.3.2 Regular waves

In Figure 4.12 to Figure 4.14 the convergence tests for the simulation of the body under regular waves can be seen. The models include springs as tested in subsection 4.2.5, to ensure similarity to the physical parameters even though some of the results are influenced negatively.
For a period of 0.8 s, it can be seen that the surge motion is largest for a mesh resolution of 10mm and smallest for a grid size of 5mm. The influence on the heave motion is small. For the pitch motion, the difference is larger. It can be seen that the coarser the grid is the larger the deviations between the crests of the same model gets.
The value of the crests in the pitch motion differs between 0.31 and 0.35 for the finest mesh, while the values range from 0.3 to 0.5 for the coarsest mesh. The period in the heave and pitch motion does not match exactly with the experimental one for all mesh variants. The period of the numerical data set is longer, leading to enlarging deviations of the extrema in time. The pitch motion also lags in the beginning, when the position of the crests in the heave motion still matches with the experimental one.
For a period of 1.2 s, a similar behaviour is observed regarding heave and pitch, but the drift is largest for the finest mesh. The influence of the resolution on heave is small again, with amplitudes being a little smaller and therefore more distant to the experiments for the finest mesh. For the pitch movement, it can again be seen that the variation is large for the coarser grid, but drastically reduced for a mesh of 5mm

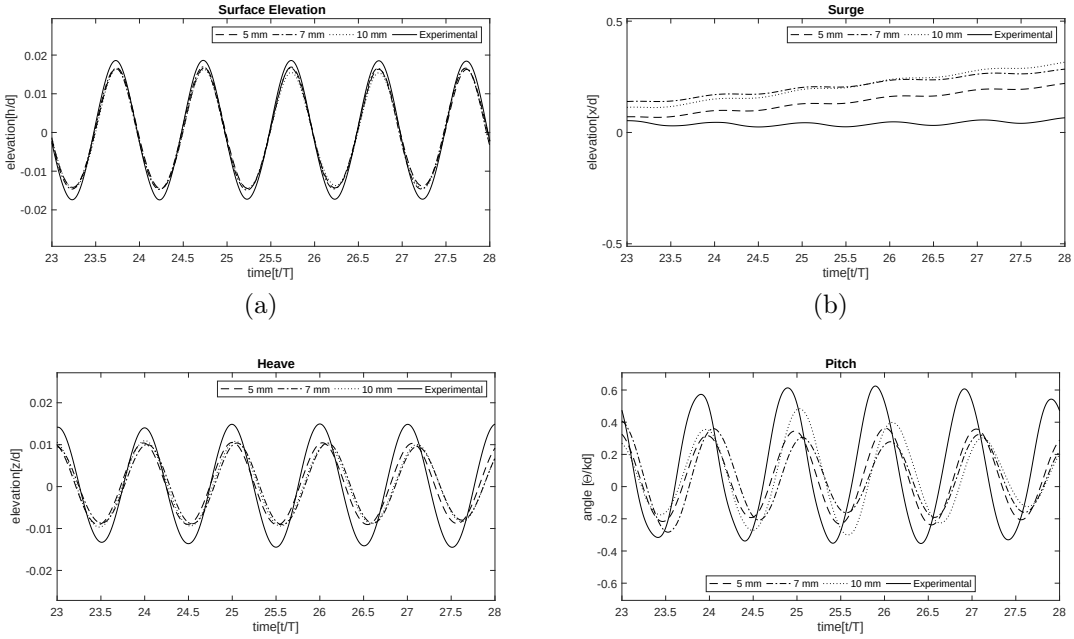

Figure 4.12: Comparison of three mesh resolutions, T=0.8s H=3cm

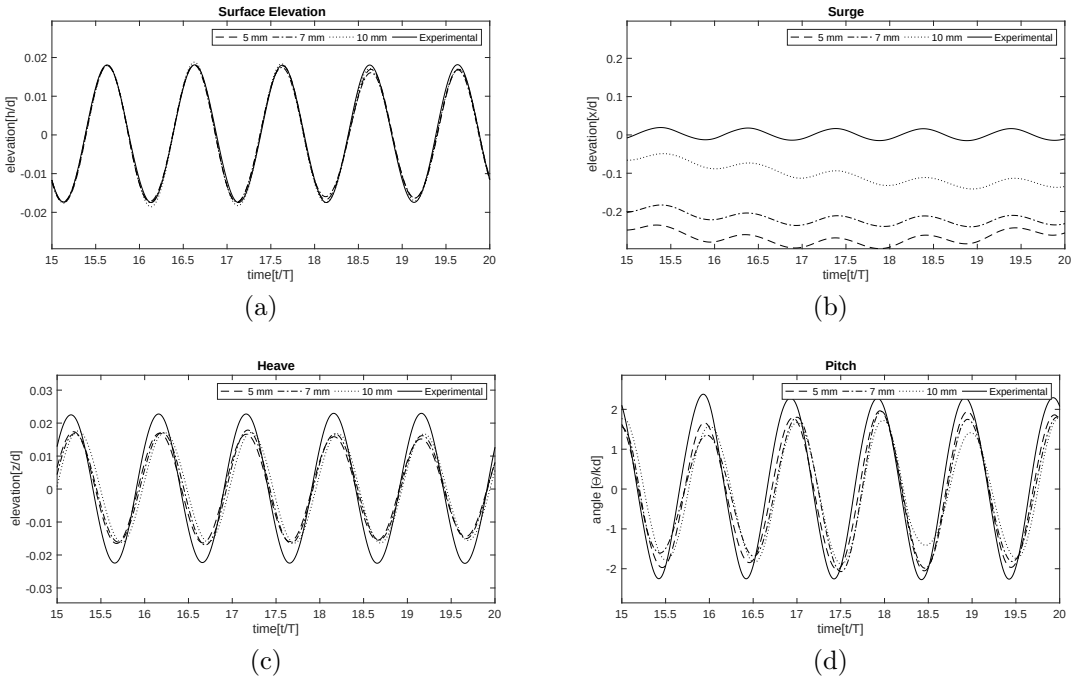

Figure 4.13: Comparison of three mesh resolutions, T=1.2 s H=3cm

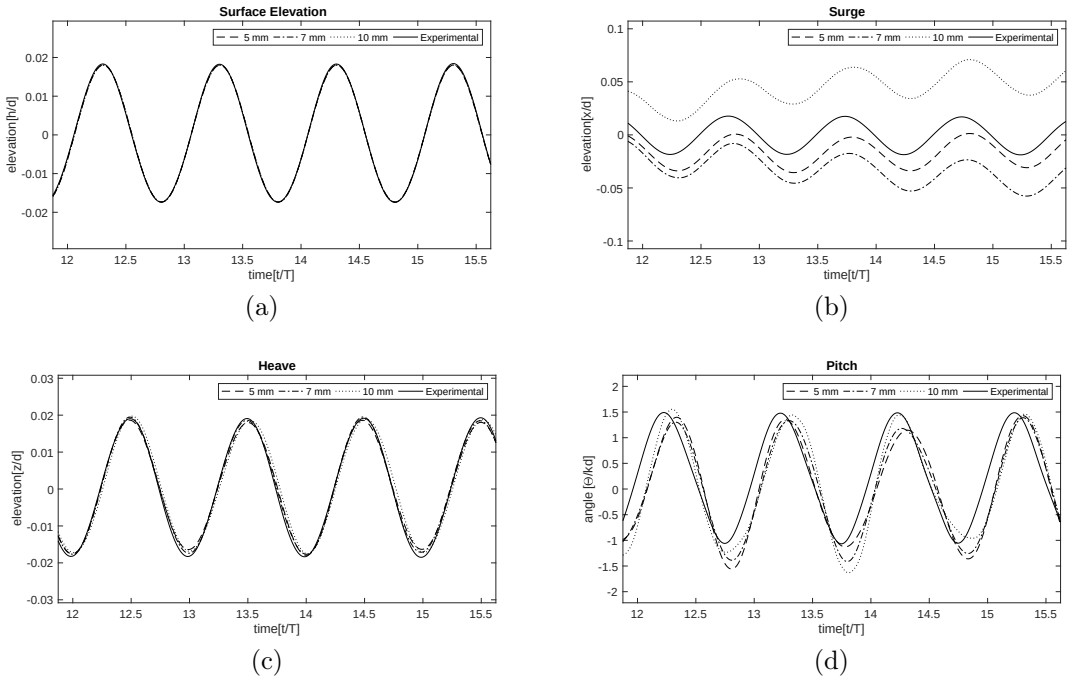

Figure 4.14: Comparison of three mesh resolutions, T=1.6 s H=3cm

and 7mm. The 5mm variant is the one closest to the experimental data here.
For waves with a period of 1.6 s, the drift motion is low for all variants but largest for a resolution of 7 mm. The difference on the heave motion is again small, but the influence is higher on the pitch motion . All the resolutions show some irregularities, especially in the troughs of the movement. The normalized angles differ between values of 1 and 1.7 for the coarsest mesh, and between 1.1 and 1.6 for the finest mesh, so that the variation is a little reduced with a higher resolved grid. The influence is not as obvious as for the other waves tested.

Chapter 5

Validation of the mooring models

5.1 Procedure

The next element to be included are the different mooring lines used. Due to the very small difference induced by the use of different spring parameters, in comparison to the deviations already existing for the free floating barge between numerical and experimental datasets, this parameter is not examined further.
Since the results are best for a waves with a period of 1.6 s and 1.2 s, these are chosen for further examination including mooring models. Not all models implemented can be used for each experimental mooring line, so different experiments are used to validate different models. The catenary equation requires parts of the mooring line to lay on the bottom. This is only the case for the chain-mooring tested, so it is used here. The quasi-static mooring is problematic regarding the neglection of the contact force to the sea floor, that is problems with modelling the chain mooring, which lays on the floor. Instead the rope mooring is used to validate this model.
Due to the fact that the numerical models are performed in only two dimensions, assumptions have to be made on how the mooring line parameters have to be adjusted. Since only a slice of the floating body is modelled, the resulting forces acting on the body are reduced. In the weakly coupled algorithm the mooring models are just taken into account as additional forces acting upon the body. It can be assumed, that the hydrodynamic forces are reduced by the share of the original width, as it was already done to include the soft-mooring springs. That means the parameters of the mooring lines need to be adapted accordingly to account for the same reduction.
The fastest way to derive the adapted parameters for the catenary equation, is by introducing two new equations. With the newly introduced parameter a the horizontal force acting upon the body results to (Faltinsen (1990)):

$$T_h = a \cdot \gamma_0, \tag{5.1}$$

The parameter a can be calculated, resulting from regrouping the following equation (Faltinsen (1990)):

$$dxy = l - dz\sqrt{(1 + 2\frac{a}{dz})} + a \cdot cos^{-1}(1 + \frac{dz}{a}). \tag{5.2}$$

All the parameters in this equation just result from geometric properties of the mooring cable, that means a is independent from the desired reduction of the force, since the geometry is not supposed to be adapted. As a consequence the resulting force upon the body solely linearly depends on the weight per unit length of the cable γ_0. This is adjusted accordingly. For a mesh of 5 mm, the acting force on the body is divided by 120 compared to the entire width of the three-dimensional prototype. To reduce the force resulting from the mooring model, the same factor is used for the weight of the line. Since only one line on each side of the body is assumed in the numerical model, the line used needs to account for two lines in the experimental models. Hence, the resulting weight needs to be multiplied by two. The resulting weight is then: $0.023kg/m \cdot \frac{2}{120} = 0.00038kg/m$.
For the rope mooring system, the same idea of accounting for the parameters in a way that the forces acting on the body are reduced, is applied. Since the weight of the line under buoyancy is negligible and with respect to the mechanisms of a rope mooring (section 1.2), the factor scaled here is the elasticity of the line. Linear behaviour of the material is assumed (Hooke's law). EA, the value required by the model for the definition of elasticity is then calculated as $c \cdot L = EA$. For the spring F2 this leads to a value of $209N/m \cdot 4.10m = 856.9N$ for the three dimensional set-up. Including the same scaling parameter as explained above this results then to a value of 14.2 N for a model with a width of 5 mm. For the spring F1 examined in the slack configuration, this leads to a value of $4.9N$ on a mesh of 5 mm.
In REEF3D, the lines are included by defining the coordinates for the attachment points on both the floor and the floating body in the ctrl-file. For both models the assumption that the fixing point on the floor is not elevated had to be introduced. Then some additional parameters are included depending on the type of model chosen. In behalf of the neglection of hydrodynamic forces, this is just the line length for the catenary model, which was given as 4.23 m, and the density which was chosen to $7850kg/m^3$, the density of steel. Elasticity was not taken into account, what can be defined by setting EA to 0.
For the quasi-static model, the density was chosen to $1001kg/m^3$ to account for the additional weight by the springs and key chains, and the line length to $4.10m$ due to the elongation induced by the lower attachment point on the bottom. Additionally, the diameter for the calculation of the hydrodynamic forces was required. This was obtained by scaling the weight known for the original rope in the same manner as for the catenary model to 0.00007 kg/m and then, calculating the diameter from

Figure 5.1: Initial position of the floating barge and the mooring chains

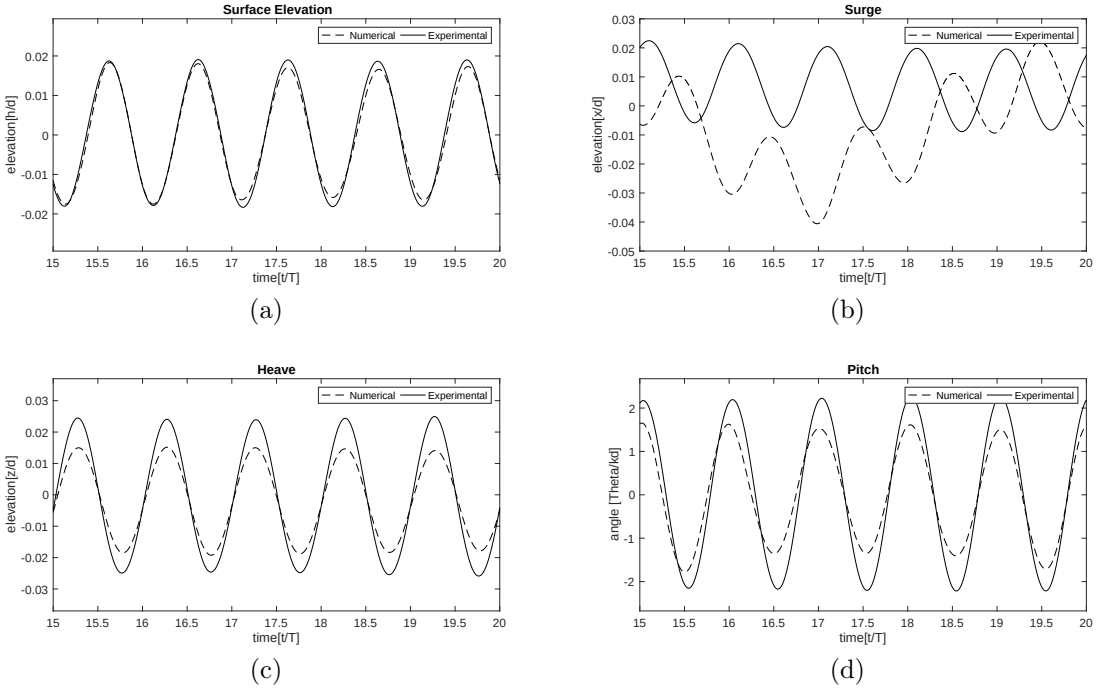

Figure 5.2: Movement of the barge using a catenary mooring model compared to experimental results (T = 1.2 s, H = 3cm)

the known density to 0.00094 m. Since the values are so small, it can be assumed, that they do not play any role and the hydrodynamic forces acting on the line are negligible. The number of elements, the line was discretized into, was chosen to be 10.

5.2 Validation of the catenary mooring model

The initial shape of the mooring lines with the parameters explained above can be seen in Figure 5.1. The resulting motion of the barge is shown in Figure 5.2 for a period of 1.2 s and in Figure 5.3 for a period of 1.6 s.
For waves with a period of 1.2 s it can be seen, that the periods of the heave and pitch motion match very well, but the amplitude is reduced compared to the experiments. The reduction is about one fourth for both of the motions. The differences for the

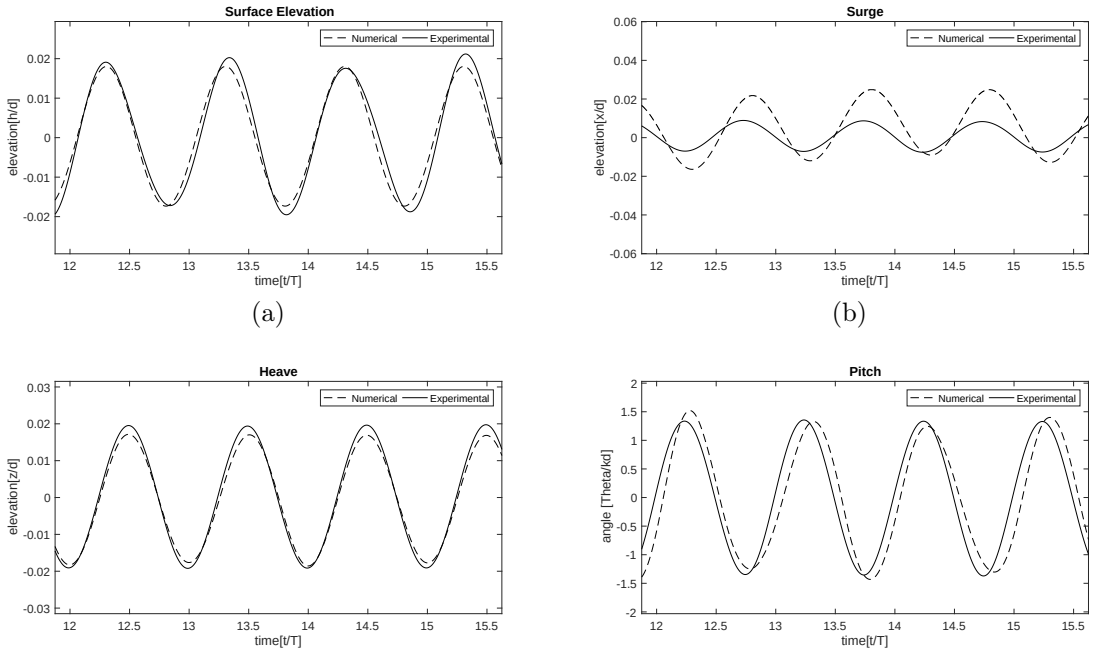

Figure 5.3: Movement of the barge using a catenary mooring model compared to experimental results (T = 1.6 s, H = 3cm)

surge motion on the other hand are significant. The motion is irregular and not even a match in the period can be observed. Compared to the free floating model under the same wave, the difference for the heave motion does not really increase, but the results for the pitch motion show larger deviations. The drift displacement that is observed in the free-floating test is not visible here.
For waves with a period of 1.6 s, the results show smaller deviations. The heave motions are very well captured with an almost perfect match of the troughs, and only slight differences in the crests. The pitch motion is also captured very well, almost no deviations in the amplitude can be observed. A small lag in the phase of the pitch can be observed. The surge amplitude is significantly overestimated by the numerical model, but in contrast to the other wave period tested the period is reproduced correctly.

5.3 Validation of the quasi-static mooring model

The quasi static mooring model was applied on the two rope mooring systems, the taut one with spring F2 one and the slack one. Each configuration was checked for two waves, T =1.2 s and T= 1.6 s. The initial position of the barge and the mooring line for the slack configuration is depicted in Figure 5.4, the one for the taut configuration

Figure 5.4: Initial position of the floating barge and the mooring ropes of a slack configuration

Figure 5.5: Initial position of the floating barge and the mooring lines of a taut configuration

in Figure 5.5.
The slack configuration does not induce a lot of change to the motion of the body (Figure 5.6 and Figure 5.7). The deviations in the heave and pitch amplitude are comparable to the ones for the free-floating barge. The surge motion is very different for both of the waves tested.
The fact, that not much change is induced by the mooring lines, leads to very good results for the 1.6 s wave and the slack configuration, since they are already very good for the free-floating configuration. The match for the heave motion is very good, the match for the pitch motion as well, even if some irregularities are observed. The surge motion is limited to a drift of a couple of centimeters in the wave direction. The amplitude of the surge motion almost matches with the one from the experimental data.
The deviations for the wave of 1.2 s in period are larger, like already given for the free-floating tests, but an overall match is given. A fact to draw the attention to is the large displacement of the barge in surge direction, here a drift of over 20 cm is observed. This matches with the displacement of the attachment point on the floor.
For the wave with a period of 1.2 s and the taut mooring (Figure 5.8) the periods of all motions are well captured. The surge motion shows some irregularities, but the overall amplitude matches. The heave amplitude is smaller than in the experiments, but the deviation is not increased compared to the free-floating results. For the pitch motion in contrast the deviations in the amplitude are large, in numbers the difference is about 1.4.
For the waves with a period 1.6 s and the taut mooring (Figure 5.9), the overall reproduction is similar. The periods match, but some deviations in the amplitudes can

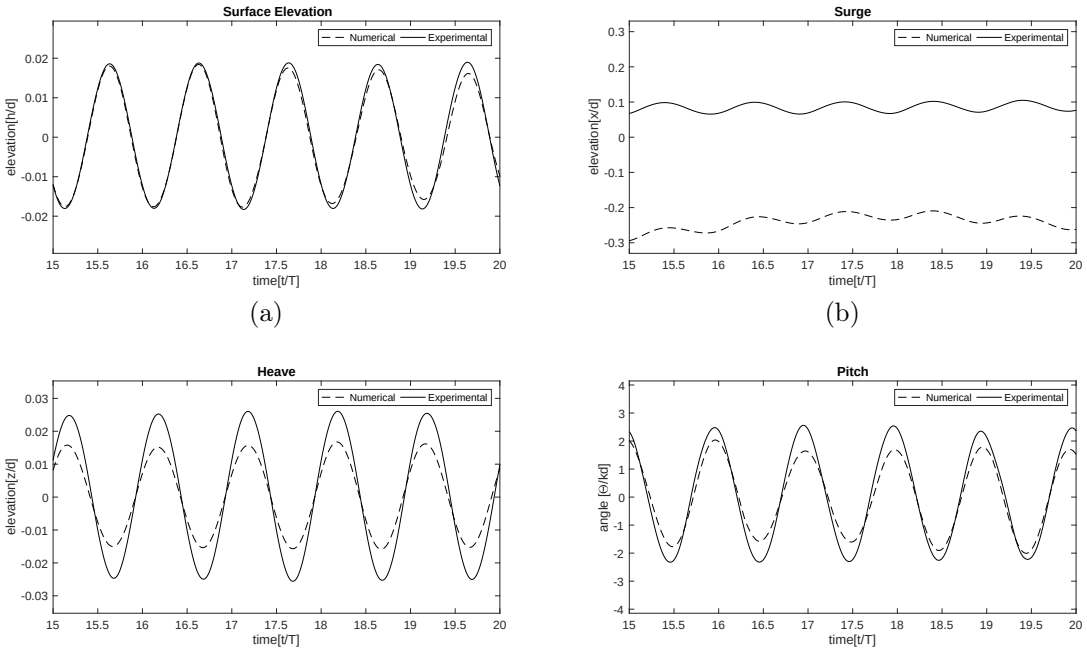

Figure 5.6: Movement of the barge using a quasi-static mooring model compared to experimental results (slack)(T = 1.2 s, H = 3cm)

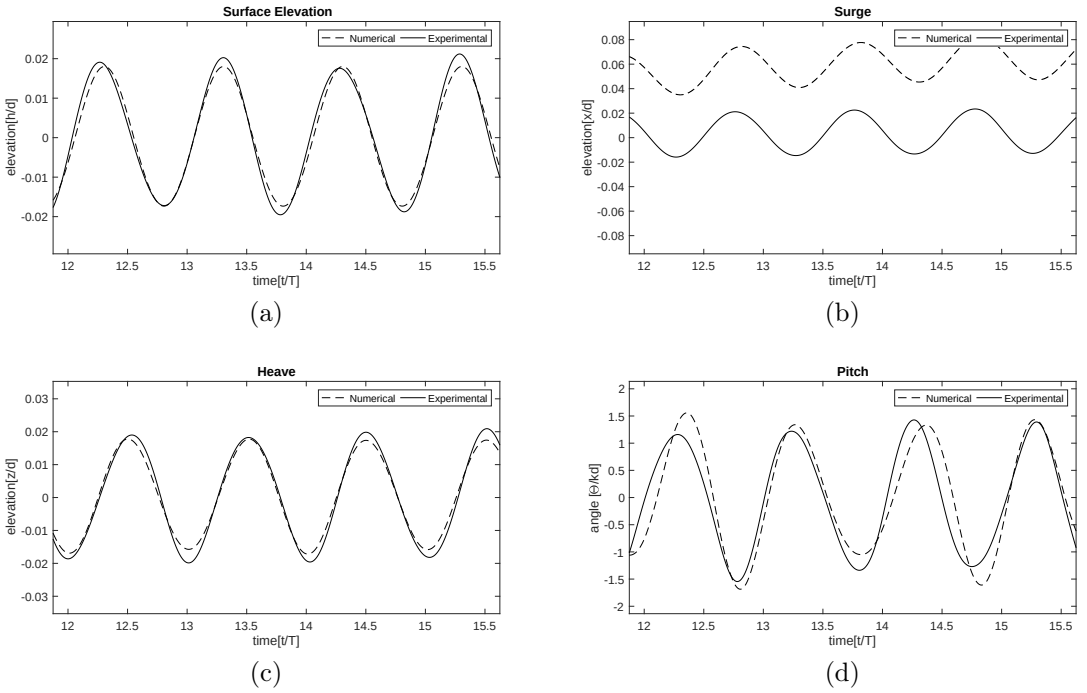

Figure 5.7: Movement of the barge using a quasi-static mooring model compared to experimental results (slack)(T = 1.6 s, H = 3cm)

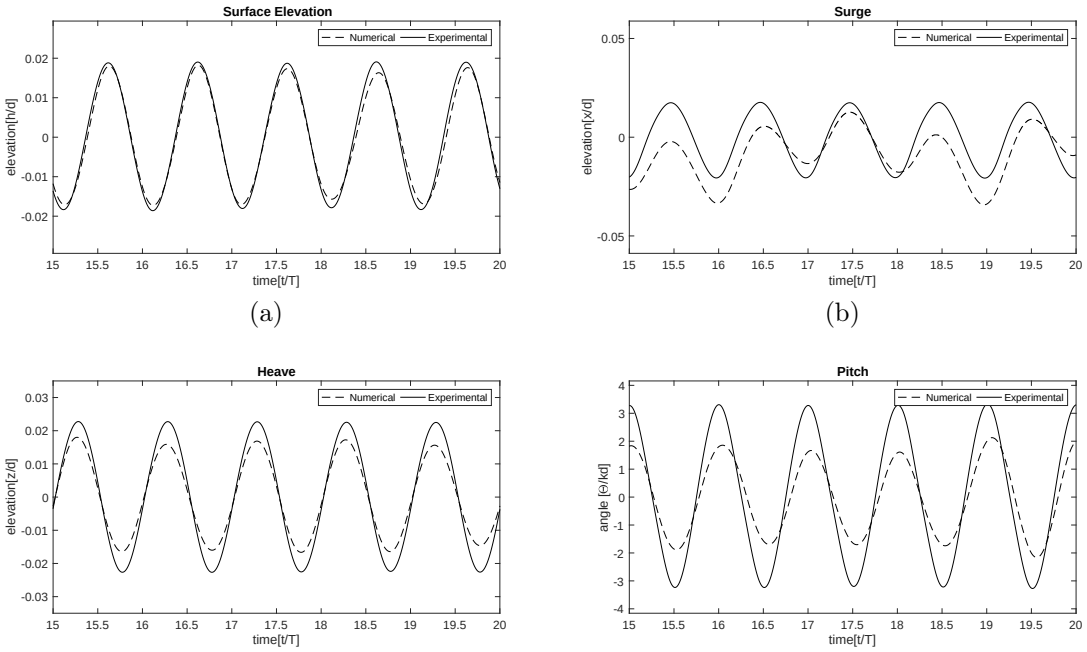

Figure 5.8: Movement of the barge using a quasi-static mooring model compared to experimental results (taut, F2)(T = 1.2 s, H = 3cm)

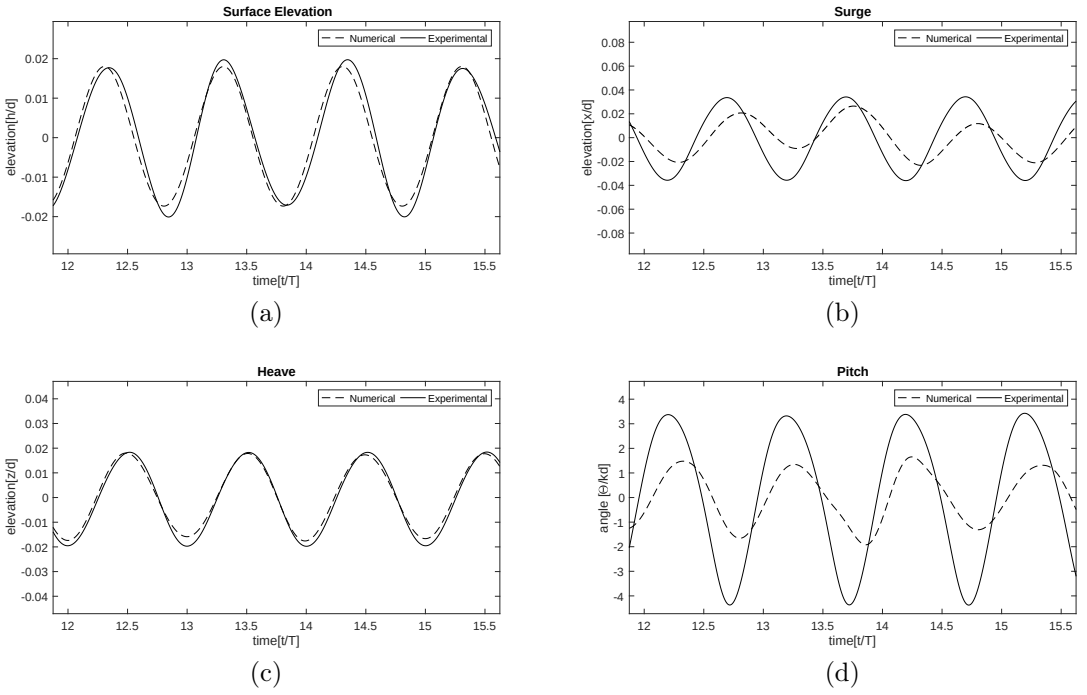

Figure 5.9: Movement of the barge using a quasi-static mooring model compared to experimental results (taut, F2)(T = 1.6 s, H = 3cm)

be observed. The surge motion is again irregular and the amplitude is a little underestimated by the numerics. The heave motion matches perfectly, but the deviations in the pitch motion are even larger. While the amplitude increases drastically in the experiments, the numerical values are about the same as in the free-floating set-up, leading to numerical values of only about a third of the experimental ones.
In order to further examine on these rather large differences between the experimental and the numerical results for a taut configuration, it is checked if the adoption of several parameters might have a positive influence on the match of the results. With regards to the fact, that the match is already good for the T = 1.2 s wave, it is the one chosen to be investigated on further.

5.4 Sensitivity analysis for the quasi-static system

Since the results for the taut quasi-static mooring model are not satisfying a sensitivity analysis was performed to examine if variations on some parameters could enhance the overall quality of the modelling results. Three different parameters were checked. This is the elasticity of the rope, the length of the rope and the vertical position of the attachment points on the barge. In addition to that, the results for the quasi-static mooring system were compared against a model, where the entire mooring lines were modelled as a set of springs. They are weightless and no hydrodynamic forces are taken into account, but since the density of the rope is so similar to water and the diameter is negligibly small in a 2D-model, very similar results were expected. The parameter that needs to be defined in addition to the geometric properties of the spring is its constraint c. That only means, that it is not multiplied with the length of the line L, as it is done to obtain EA, which results in a value of $3.5N/m$.
The motion under the use of the springs is shown in comparison to the solution with the use of the quasi-static model in Figure 5.10. The reproduction of the motion reduces drastically with this model applied. The introduction has a significant influence on the wave gauge, reducing the elevation on some peaks. The peaks of the heave motion are also reduced, while the troughs stay mostly constant. The largest influence can be observed on the pitch motion, where strong irregularities occur. In some parts the amplitude is increased, so that it matches with the experimental data, in some parts it is reduced to significantly lower values than for the quasi-static one.
In Figure 5.11, the movement of the barge for the different elasticity-parameters is shown. It can be seen, that a reduction of the stiffness leads to higher amplitudes for the pitch motion, which reduces the deviation to the experimental data. On some points of the heave motion an increase can also be observed with the increase of the elasticity, but here no general trend can be seen. The surge motion is more difficult to compare, since the amplitude of motion is irregular in both cases. The change of

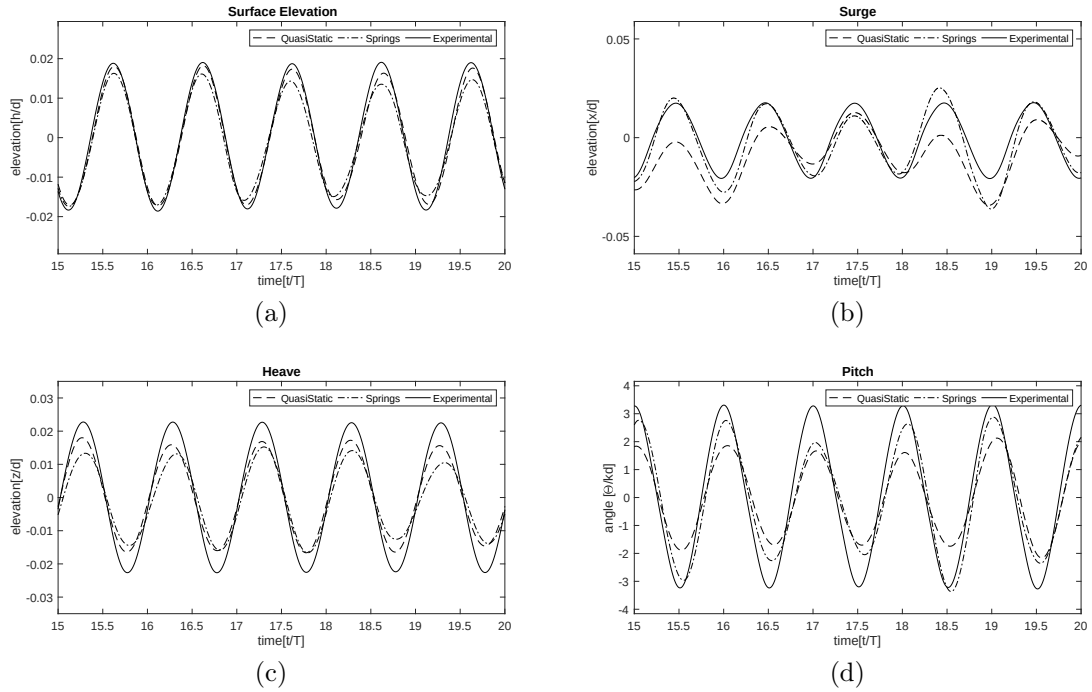

Figure 5.10: Movement of the barge using a quasi-static mooring model and the spring model compared to experimental results (taut, F2)(T = 1.2 s, H = 3cm)

elasticity leads to a drastically altered motion in this direction, with differences of several cm and completely different trends in the motion.
The comparison of two different line lengths in Figure 5.12 shows only a small influence of the line length on the motion. The heave motion is barely affected. The pitch motion reveals some deviations with larger amplitudes, when the longer rope is used between 16.5 and 18.5, but reduced amplitudes for this variant on the end of the examined time series. In the surge motion, a large influence can be observed. At the beginning of the window examined, a large displacement for the longer rope is observed, which is reduced later in time, but still the motions of the two numerical experiments never match and are much more volatile than the results from the physical experiments.
The model shows to be highly sensitive to changes on the location of the attachment points, as can be seen in Figure 5.13. The surge motion is again irregular, and shows completely different development for all variants tested. No clear trend of how this motion is affected by the changed attachment points can be determined. The heave motion is only slightly affected, the amplitude with higher attachment points is decreased in some points. Again a large effect can be observed on the pitch motion. Here, a change of the attachment points leads to highly irregular movements. In some points the amplitude is increased in some points decreased for both directions

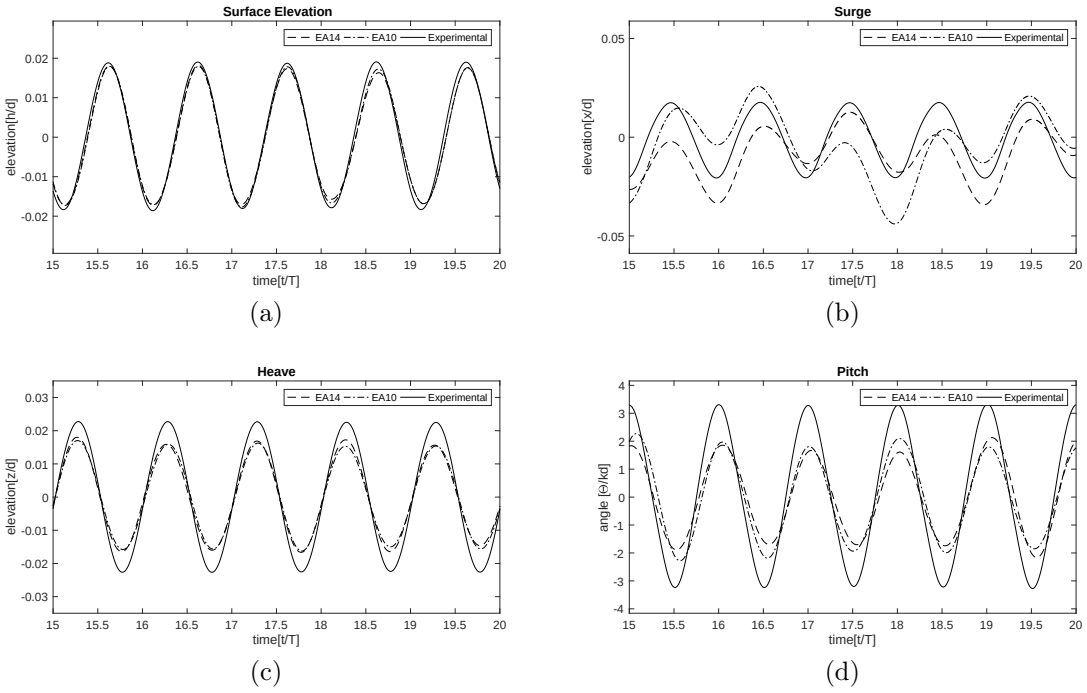

Figure 5.11: Movement of the barge using a quasi-static mooring model for two different values of EA compared to experiments (taut, F2)(T = 1.2 s, H = 3cm)

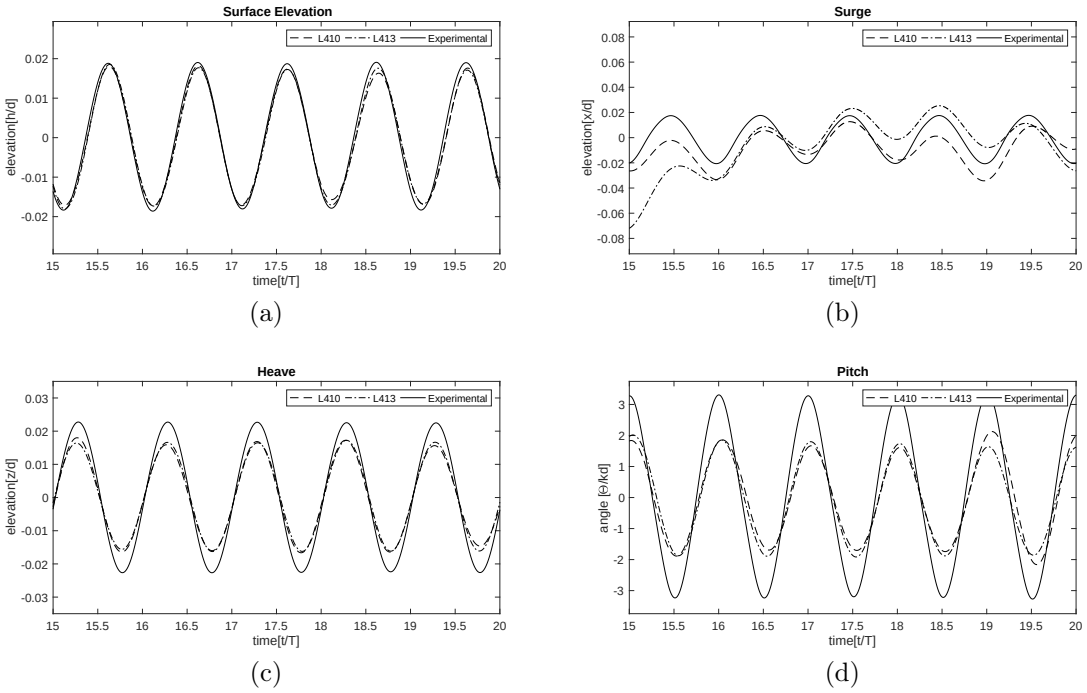

Figure 5.12: Movement of the barge using a quasi-static mooring model for two different line lengths compared to experiments (taut, F2)(T = 1.2 s, H = 3cm)

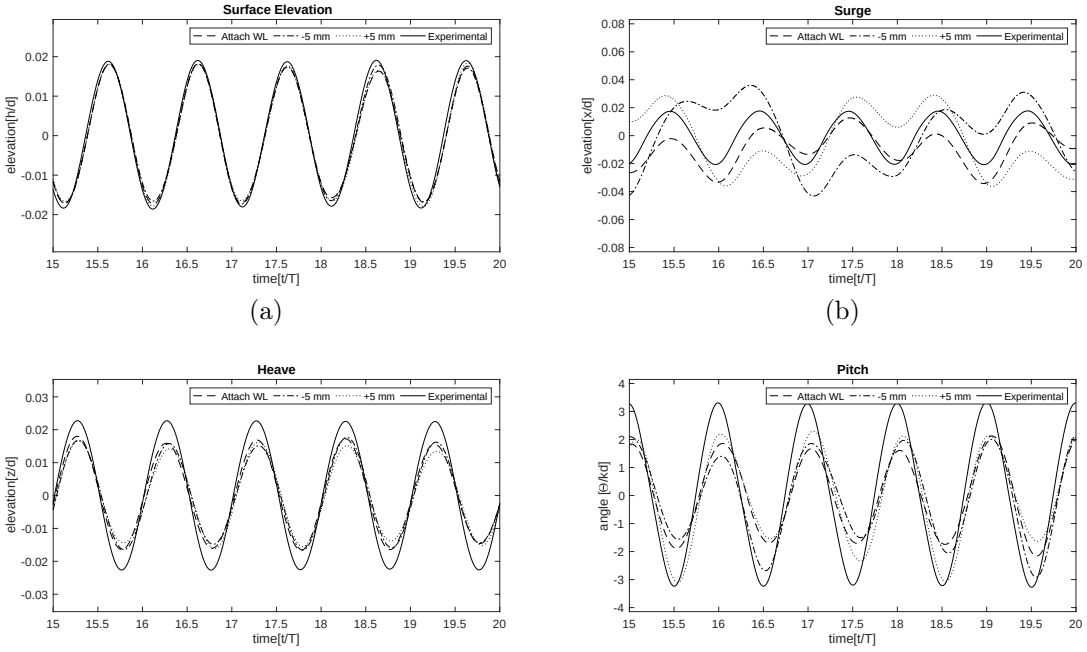

Figure 5.13: Movement of the barge using a quasi-static mooring model for different vertical positions of the attachment points on the box (taut, F2)(T = 1.2 s, H = 3cm)

of replacement of the attachment points. The match to the experimental data is very good on some points, but also very bad on others.

Chapter 6

Discussion

6.1 Free-floating barge

While comparing the numerical results to the experimental ones, it has of course to be considered, that the experimental results also include errors, induced for example by the instruments, by small irregularities of the materials used or imprecision in the set-up of the model. In this light especially the mooring lines added are prone to errors due to many possible deviations from the planned set-up. The exact positioning of the attachment points on the floor, as well as the exact length of the lines were difficult to adjust. That is a reason for why the influence of those parameters changing were finally included in a parameter study.
However, the regular motion in most of the experimental set-ups is a clear sign, that the overall quality is high and only small errors may be induced in the exact amplitudes of the single movements. Naturally the possibility of errors does not mean that, they are necessarily favourable for the comparison of the results. It could also be that the deviation gets smaller caused by a small error in the experimental results. The only wave, where some irregularities could be observed, is the one with T = 0.8 s for the free-floating body. Here the crests and troughs differ periodically over time. It is not clear if this a physical behavior or if the rapidly moving barge limited exact capturing of its movement (see appendix).
The quality of reproduction of the CFD solver differs for the different waves tested. The deviations arise in different aspects of the reproduction, so that a differentiation is made and the waves are discussed separately. A problem was the drift motion induced. For the numerical reproduction, a completely free floating barge would have been favourable due to the reduction of unknown parameters then. In the tested scale and the given facilities this is not possible due to the fact, that a free floating barge could damage instruments, itself or just drift out of the area, that is covered by the tracking cameras. Consequently the limits of the physical world need to be accepted,

and taken into account within the numerical modelling.
The spring's influence depends on the initial drift motion without springs. For the wave with a period of 1.6 s, the waves did not induce drift motion, so that an inclusion of the springs did not lead to an altered behaviour of the box. In contrast to that, both of the other waves did show differences in their heave and pitch motion, with springs included while this was explicitly not the case for the physical models. The basis for the introduction of the soft-mooring system was the fact of having no influence on these two motions. In addition to that, the physically scaled introduction of the springs did not show the intended effect on the surge motion of the barge. With the chosen values they were not able to reproduce the stationkeeping given in the experiment. Maybe this could have been overcome by increasing the stiffness of the spring, but then no physical basis for the parameter would have existed anymore and a danger of overcalibrating would arise.
Another point in this context is the runtime of the model, with increasing length of the springs an increasing force on the body would be induced, while the drift force stays constant. At a certain point this would have led to a movement against the wave direction. A tendency of this could already be seen when a larger timeseries is studied (Appendix). To really allow for a surge motion in equilibrium, a much larger timeseries would have had to be examined, with the effect, that the size of the wave tank would probably also have had to be increased to prevent reflecting waves from interfering. In consequence, an examination of this was not possible due to the limitations of computational power.
The resolution of the grid had a similar influence on the models under all waveloads. The heave motion in the algorithm seems to be not to strongly affected by the resolution of the cells, while the pitch motion seems to be very sensitive to the resolution. This seems convincing since the pitch motion is determined by small scale influences, like the exact capturing of the edges of the barge. In contrast to that, we do not see that much of an influence in the pitch decay tests, while in the heave decay-test the correct period was only captured in a mesh of 5 mm resolution. In regular waves the effect was rather on the regularity of the motion, that was expected from the harmony of the attacking forces and supported by showing the exact same behavior in the experiments, than on the exact values. Different from the decay-tests, the period was captured well in use of all mesh resolutions.
The exact match between the numerical data for the finest mesh and the experimental data seems generally satisfying, for all of the waves examined. The quality of the match is improving with growing wave period. It has to be kept in mind that the normalization leads to a different scale for the pitch amplitude, with values of the numerical model ranging about 2° for the waves T=0.8 s and T = 1.6 s and an absolute value of about 5° for wave T = 1.2 s. That also means that the different quality of reproduction is not connected to the absolute value of the movement, but

the period seems to have a direct impact.
Considering the possible errors in the experiments some deviation in the exact amplitudes seems acceptable. The change of the periods is in agreement with the drift motion of the body. In this context the drifting against the wave direction for a the wave T = 1.2 s arises questions, since this is not the direction expected. Furthermore it has again to be stressed, that the floating algorithm could not be tested isolated, but only with the springs included, which makes it more prone to the inclusion of errors. Even though the absolute values for the wave with a period of 1.6 s are the best matching ones, the attention should be drawn to the fact the the algorithm produces irregularities in the pitch motion, no matter if the springs are included or not. This is a behaviour clearly not physical, and can not be explained by small deviations in the set-up, since the numerical input is absolutely harmonic and symmetric.

6.2 Catenary mooring model

The overall match of the results for the numerical data generated in use of the catenary model is also satisfying, taking into account the already existing deviations for the calculation of the free-floating barge. The existing deviations from the floating algorithm make the comparison more difficult, but still the tendency of the influence of the mooring can be evaluated on. Since here the deviations in the setup introduced by the springs do not account anymore, the surge motion is expected to be more precisely reproduced.
Again the quality of the results increases with the length of the waves used. For the wave T=1.2 s both, heave and pitch motion are damped more when the mooring model is applied, but the difference is rather small, so the match of the data is still acceptable. However the experiments don't show such a behaviour. It was expected, that the mooring model had no influence on the amplitudes. The surge motion is completely of the expected values, this might be an explanation for the damping of the two other motions.
The results of the 1.6 s wave even improve with the use of the catenary model. The change in the heave motion is small but the tendency is also of introducing an additional damping, while the experiments showed the opposite influence. The main drawback in the reproduction of the results for this wave in the free-floating case can not be observed anymore. This is, the irregularities in the pitch motion disappear, while still showing a good match in the amplitude. This is surprising, since it occurred in both the free floating and the soft-mooring system, so the effect can not be explained by the use of springs. The deviation in time exist the same way as before, indicating that this is a general problem of the floating algorithm in reproducing the motion for the given wave. An aspect that clearly needs to be

addressed in the future is the surge motion, which is not reproduced as desired.

6.3 Quasi-static mooring model

To evaluate on the reproduction with this mooring model applied, the tendency induced in the experiments needs to be kept in mind. The slack mooring configuration barely leads to any change in the motion, while the taut configuration increases the pitch amplitude drastically, especially for a wave of 1.6 s.
The results are good for a wave of 1.6 s and a slack configuration, acceptable for both configurations for a wave of 1.2 s and unsatisfying for the taut configuration for the 1.6 s wave. The largest deviations in between the experiments and their reproduction become manifest in the pitch motion, so exactly in the motion, where the taut mooring lines have the largest influence in the experiments. In the numerical results no such influence of the different mooring configuration is observed. The motion stays almost unaffected for all configurations. For that reason the match for the slack test are very similar to the match for the free-floating body.
Regardless of the absolute match of the data at least a qualitative influence on motion should be observed. In this case that would be an increase in the pitch amplitude induced by the taut mooring model. Here in the examined tests no increase of the pitch motion induced by the mooring model can be observed at all. That means the main feature of the taut mooring system is not captured. In order to check if this could be induced by some variations in the experimental tests or the wrong choice of several parameters in the set-up of the numerical model the sensitivity analysis was performed, which is discussed below.

6.4 Sensitivity of the quasi-static mooring model

An influence that clearly has a positive effect on the reproduction is the reduction of the stiffness of the mooring line EA. This leads to an increase in the amplitude of the pitch motion, which is the result that was desired. The strong effect on the surge motion is another aspect that requires further investigation. The model does not seem to be very sensitive to the line length, as this has no large influence on the motion.
Other aspects don't show such an obvious tendency. Both, the use of springs as well as the change of position of the attachment points lead to an irregular motion. The influence of the displacement of the attachment points was not checked in experiments, but it seems highly questionable that a symmetric change would alter the motion in such a way. In the light of the numerical results showing such irregularities in other cases as well, it rather seems to be connected to the solver.

The deviations induced by the springs to model the same set-up further rise suspicions regarding the numerical solution. The difference can not be explained by the different model assumptions as the differences were expected to be negligible as explained. The irregularities in the solution under use of the springs, makes the quasi-static solution seem more trustworthy. In any case the deviation in between the results is clearly another topic, that should be investigated further on, at least one of the models produces results that are not reliable.
Overall the quasi-static mooring model can not be validated. The heave motion is predicted well and does not show to be very sensitive to changes on the mooring line, but the pitch and the surge motion are not reproduced satisfyingly. It can not reproduce the increase in pitch amplitudes for a taut mooring system that are induced in the experiments and reacts very sensitive to changes upon the line's parameters regarding the pitch and surge motions. For cases where the mooring lines don't have a large influence, namely the slack configuration, the results are still very good.

Chapter 7

Conclusion and Outlook

Numerical tools are a fast an efficient way to calculate the response of floating structures to waves, but they need benchmark data to validate the quality of their prediction. Taking into account the reduced complexity of generic cases with simple geometric forms, they are a good starting, point for the validation of the numerical tools. In this thesis, an existing dataset for a floating wooden box of constant density was extended, adding different configurations of mooring lines to ensure the stationkeeping. The configurations included a chain and a rope mooring, tested in a taut and a slack status, as well as the use of different springs to account for different elastic parameters. All additional configurations were tested under regular waves ranging between 0.8 s and 1.6 s in period and 2 cm and 3 cm in height. This benchmark data now allows for different CFD codes to test their floating and mooring algorithms.
In this work, this was done for REEF3D, a solver for the RANS-equations relying on a finite differences approach, developed at the department of marine civil engineering at the NTNU in Trondheim, Norway. The solver includes a weakly coupled floating algorithm based on ghost-cell immersed boundary approach. Furthermore three different mooring models are included to account for the effect of different mooring configurations, taking into account a varying number of environmental loads. In this thesis a catenary approach and a quasi-static one were tested. For the validation, the set-up was reproduced in a 20 m long numerical wave tank provided by the code. In order to save computational expenses, the calculations were done in only two dimensions.
An issue was the stationkeeping of the barge using a soft-mooring system in the experiments. To reproduce the lack of a drift motion in the numeric set-up, soft-springs were introduced here as well. This influenced some results negatively, but was nonetheless applied to ensure proximity to the experimental set up. For the free-floating barge, the result are generally satisfying. The quality increases with increased period. All the motions are under-predicted by the solver except for the 1.6 s wave where a match is obtained. The pitch motion shows to be more sensitive, here an irregular movement can be observed in some cases. These irregularities are reduced

with the use of a higher resolved grid.
In a next step, the catenary mooring model is validated using the data from the chain as mooring lines. Due to the reduction of dimensions, the parameters had to be adapted. Hence, the weight of the mooring line was divided by the share of the 2D body of the original width, to reduce the acting forces on the body. The mooring line does not show to have a large influence, as was already expected by the experimental results. Consequently the match is very well for the 1.6 s wave, but the motion is underestimated for the 1.2 s wave. With the mooring model no more drift influences can be seen, but the surge motion is overestimated.
The quasi-static mooring model is compared against experimental data from the rope as a mooring line. Both, a taut and a slack configuration are tested. Here, the elasticity of the line was reduced to account for the two dimensional model. Again, the mooring line showed to have only a small influence on the body. This led to good results for the slack mooring, where the experimental influence was also small. The taut mooring induced a significant increase in the pitch amplitude in the experiments which could not be reproduced by the numerical model. In order to further examine this, the sensitivity of various parameters was checked. Here the reduction of the stiffness showed to have a positive impact, but irregularities induced by a change of the vertical position of the attachment points on the box and the use of the spring models for the mooring lines arose further questions instead of providing clarity. Overall the model could therefore not be validated, since the main effect, the induction of higher pitch amplitudes in a taut configuration could not be reproduced.
Further research is especially required in the accurate prediction of the surge motion, since here independent from the mooring system largest deviations could be observed. In cases that showed accurate prediction of the surge motion, the other motions were also well predicted. This indicates a correlation in the movements.
With the existence of the benchmark data, all improvements implemented in the code now can directly be tested in terms of reproduction of the experiments. Even though the floating solver shows good results, the match especially for shorter waves should still be improved. The catenary mooring shows generally good results, regarding the deviation already existing from the isolated free-floating solution, but the surge motion is not predicted accurately. Hence, further investigation is required to predict this motion precisely. The quasi-static mooring model requires revision, since it does not reproduce the effect on the motion for cases, where the mooring set-up alters the movement.
Experimental and numerical modelling are a powerful couple. The data-set generated can be used for the validation of various CFD-codes. The existing data set allows for some more features of the solvers also to be tested. But as mentioned the influence of different inertia was also tested for the free-floating barge in the experiments, and it should be checked if the solver can handle this input. Numerous extensions of the

benchmark data are also possible to bring it stepwise closer to the complex cases used in real applications and therefore allow for the code to be used for practical purposes. This could be the examination of different attachment points on the box, different geometries of the barge, different scales of the model or different densities.

Bibliography

Agency, I.E. (2018). Offshore energy outlook.

Bento, N. and Fontes, M. (2019). Emergence of floating offshore wind energy: Technology and industry. *Renewable and Sustainable Energy Reviews*, **99**, 66 – 82. ISSN 1364-0321. doi:https://doi.org/10.1016/j.rser.2018.09.035.

Bergdahl, L., Palm, J., Eskilsson, C. and Lindahl, J. (2016). Dynamically scaled model experiment of a mooring cable. *Journal of Marine Science and Engineering*, **4**, 5. doi:10.3390/jmse4010005.

Berthelsen, P.A. and Faltinsen, O.M. (2008). A local directional ghost cell approach for incompressible viscous flow problems with irregular boundaries. *Journal of Computational Physics*, **227**(9), 4354 – 4397. ISSN 0021-9991. doi:https://doi.org/10.1016/j.jcp.2007.12.022.

Bihs, H. (2018). Reef3d - user guide 18.06. Technical report.

Bihs, H. and Kamath, A. (2017). A combined level set/ghost cell immersed boundary representation for floating body simulations. *International Journal for Numerical Methods in Fluids*, **83**(12), 905–916. doi:doi:10.1002/fld.4333.

Bihs, H., Kamath, A., Chella, M.A., Aggarwal, A. and Arntsen, Ø.A. (2016). A new level set numerical wave tank with improved density interpolation for complex wave hydrodynamics. *Computers & Fluids*, **140**, 191 – 208. ISSN 0045-7930. doi:https://doi.org/10.1016/j.compfluid.2016.09.012.

Blažauskas, N., Pašilis, A. and Knolis, A. (2015). Potential applications for small scale wave energy installations. *Renewable and Sustainable Energy Reviews*, **49**, 297 – 305. ISSN 1364-0321. doi:https://doi.org/10.1016/j.rser.2015.04.122.

Brown, D.T. (2005). Chapter 8 - mooring systems. In: S.K. CHAKRABARTI (Editor), *Handbook of Offshore Engineering*, 663 – 708. Elsevier, London. ISBN 978-0-08-044381-2. doi:https://doi.org/10.1016/B978-0-08-044381-2.50015-1.

Chorin, A.J. (1968). Numerical solution of the navier-stokes equations. *Mathematics of Computation*, **22**(104), 745–762. ISSN 00255718, 10886842.

Christensen, E.D., Bingham, H.B., Friis, A.P.S., Larsen, A.K. and Jensen, K.L. (2018). An experimental and numerical study of floating breakwaters. *Coastal Engineering*, **137**, 43 – 58. ISSN 0378-3839. doi:https://doi.org/10.1016/j.coastaleng.2018.03.002.

Durst, F. (2006). Potentialströmungen. In: *Grundlagen der Strömungsmechanik*. Springer, Berlin, Heidelberg.

Ernst and Young (2017). The norwegian aquaculture analysis 2017. Technical report.

Faltinsen, O. (1990). *Sea Loads on Ships and Offshore Structures*.

Ferziger, J.H. and Perić, M. (2008). *Numerische Strömungsmechanik*. SpringerLink : Bücher. Springer Berlin Heidelberg, Berlin, Heidelberg. ISBN 978-3-540-68228-8. doi:10.1007/978-3-540-68228-8.

Fitzgerald, J. and Bergdahl, L. (2008). Including moorings in the assessment of a generic offshore wave energy converter: A frequency domain approach. *Marine Structures*, **21**(1), 23 – 46. ISSN 0951-8339. doi:https://doi.org/10.1016/j.marstruc.2007.09.004.

Fossen, T.I. (1994). *Guidance and control of ocean vehicles*. John Wiley & Sons Inc.

Griebel, M., Dornseifer, T. and Neunhoeffer, T. (1998). Numerical simulation in fluid dynamics: A practical introduction. doi:10.1137/1.9780898719703.

Hackmann, W. (1983). Mathematische begründung von verfahren zur berechnung von form und zugkraft in fadenzugsystemen. *ZAMM - Journal of Applied Mathematics and Mechanics / Zeitschrift für Angewandte Mathematik und Mechanik*, **63**(3), 173–184. doi:doi:10.1002/zamm.19830630305.

He, F., Huang, Z. and Law, A.W.K. (2012). Hydrodynamic performance of a rectangular floating breakwater with and without pneumatic chambers: An experimental study. *Ocean Engineering*, **51**, 16 – 27. ISSN 0029-8018. doi:https://doi.org/10.1016/j.oceaneng.2012.05.008.

Jacobsen, N.G., Fuhrman, D.R. and Fredsøe, J. (2012). A wave generation toolbox for the open-source cfd library: Openfoam®. *International Journal for Numerical Methods in Fluids*, **70**(9), 1073–1088. doi:doi:10.1002/fld.2726.

Ji, C.Y., Chen, X., Cui, J., Gaidai, O. and Incecik, A. (2016). Experimental study on configuration optimization of floating breakwaters. *Ocean Engineering*, **117**, 302 – 310. ISSN 0029-8018. doi:https://doi.org/10.1016/j.oceaneng.2016.03.002.

Jiang, G.S. and Shu, C.W. (1996). Efficient implementation of weighted eno schemes. *Journal of Computational Physics*, **126**(1), 202 – 228. ISSN 0021-9991. doi:https://doi.org/10.1006/jcph.1996.0130.

jr. Oertel, H., Böhle, M. and Reviol, T. (2015). *Strömungsmechanik für Ingenieure und Naturwissenschaftler*, volume 7. Auflage. Springer Vieweg.

Laurien, E. and Oertel, H. (2018). *Numerische Strömungsmechanik : Grundgleichungen und Modelle - Lösungsmethoden - Qualität und Genauigkeit*, volume 6. Auflage. Springer Vieweg.

M J Journée, J. and W Massie, W. (2001). *Offshore Hydromechanics*.

Martin, T., Kamath, A. and Bihs, H. (2018*a*). *Modelling and Simulation of Moored-floating Structures using the Tension-Element-Method*, volume 2. ASME 2018 37th International Conference on Ocean, Offshore and Arctic Engineering.

Martin, T., Kamath, A. and Bihs, H. (2018*b*). Numerical simulation of interactions between water waves and a moored-floating breakwater. *Coastal Engineering Proceedings*, **1**(36), 105. ISSN 2156-1028. doi:10.9753/icce.v36.papers.105.

Martin, T., Schacht, S., Riesen, P. and Paschen, M. (2018*c*). Efficient implementation of a numerical model for flexible net structures. *Ocean Engineering*, **150**, 272 – 279. ISSN 0029-8018. doi:https://doi.org/10.1016/j.oceaneng.2017.12.064.

Mayer, S., Garapon, A. and Sørensen, L.S. (1998). A fractional step method for unsteady free-surface flow with applications to non-linear wave dynamics. *International Journal for Numerical Methods in Fluids*, **28**(2), 293–315.

Menter, F. (1993). Zonal two equation k-w turbulence models for aerodynamic flows. *AIAA Paper*, **1993**. doi:10.2514/6.1993-2906.

Meyer, J. (2018). Physical and numerical simulation of floating bodies. In: *Master thesis - Leibniz Universität Hannover*.

Osher, S. and Sethian, J.A. (1988). Fronts propagating with curvature-dependent speed: Algorithms based on hamilton-jacobi formulations. *Journal of Computational Physics*, **79**(1), 12 – 49. ISSN 0021-9991. doi:https://doi.org/10.1016/0021-9991(88)90002-2.

Ren, B., He, M., Dong, P. and Wen, H. (2015). Nonlinear simulations of wave-induced motions of a freely floating body using wcsph method. *Applied Ocean Research*, **50**, 1 – 12. ISSN 0141-1187. doi:https://doi.org/10.1016/j.apor.2014.12.003.

Sannasiraj, S., Sundar, V. and Sundaravadivelu, R. (1998). Mooring forces and motion responses of pontoon-type floating breakwaters. *Ocean Engineering*, **25**(1), 27 – 48. ISSN 0029-8018. doi:https://doi.org/10.1016/S0029-8018(96)00044-3.

Schlichting, H. (1979). *Boundary-layer theory*. New York: McGraw-Hill.

Shu, C.W. and Osher, S. (1988). Efficient implementation of essentially non-oscillatory shock-capturing schemes. *Journal of Computational Physics*, **77**(2), 439 – 471. ISSN 0021-9991. doi:https://doi.org/10.1016/0021-9991(88)90177-5.

Sulaiman, O., Magee, A., Bahrain, Z., Kader, A., Maimun, A., Pauzi, A., Nick, W.W. and Othman, K. (2013). Mooring analysis for very large offshore aquaculture ocean plantation floating structure. *Ocean & Coastal Management*, **80**, 80 – 88. ISSN 0964-5691. doi:https://doi.org/10.1016/j.ocecoaman.2013.02.010.

Sussman, M., Smereka, P. and Osher, S. (1994). A level set approach for computing solutions to incompressible two-phase flow. *Journal of Computational Physics*, **114**(1), 146 – 159. ISSN 0021-9991. doi:https://doi.org/10.1006/jcph.1994.1155.

van der Vorst, H. (1992). Bi-cgstab: A fast and smoothly converging variant of bi-cg for the solution of nonsymmetric linear systems. *SIAM Journal on Scientific and Statistical Computing*, **13**(2), 631–644. doi:10.1137/0913035.

Wilcox, D.C. (2006). Turbulence modeling for cfd. *Turbulence Modeling for CFD*, **2**.

Yang, J. and Stern, F. (2013). Robust and efficient setup procedure for complex triangulations in immersed boundary simulations. *Journal of Fluids Engineering*, **135**, 101107 0098–2202.

List of Figures in Appendix

A.1 A motion-tracking camera 75
A.2 Picture of the ring for attaching the soft-mooring system 76
A.3 The barge 77
A.4 Two wave gauges 78
A.5 The weight-ballasted attachment points on the floor 79

B.1 Long term periodic motions of the free-floating barge in the experiments (T = 0.8 s, H = 3cm) 80
B.2 Long time modelled time series including springs (T = 0.8 s, H = 3cm) 81

Appendix A

Photographies of the experimental set-up

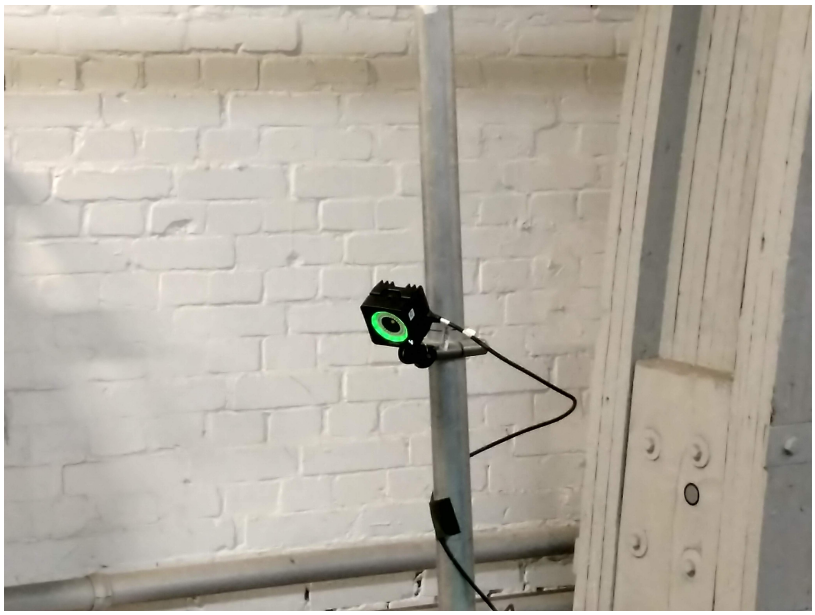

Figure A.1: A motion-tracking camera

Figure A.2: Picture of the ring for attaching the soft-mooring system

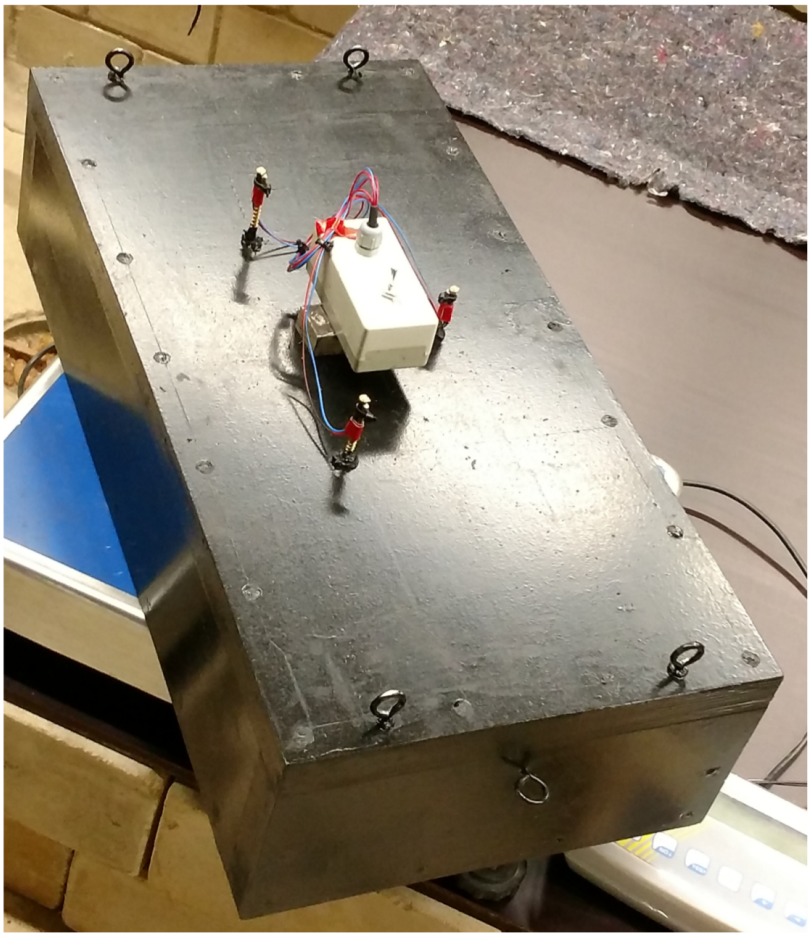

Figure A.3: The barge

Figure A.4: Two wave gauges

Figure A.5: The weight-ballasted attachment points on the floor

Appendix B

Long term time series

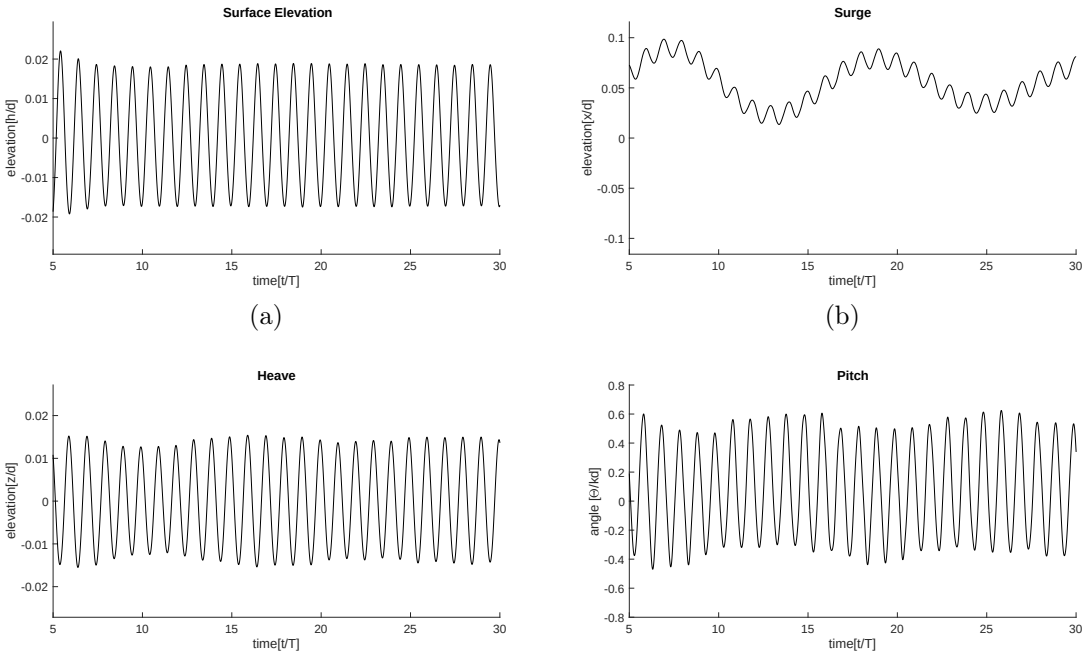

Figure B.1: Long term periodic motions of the free-floating barge in the experiments (T = 0.8 s, H = 3cm)

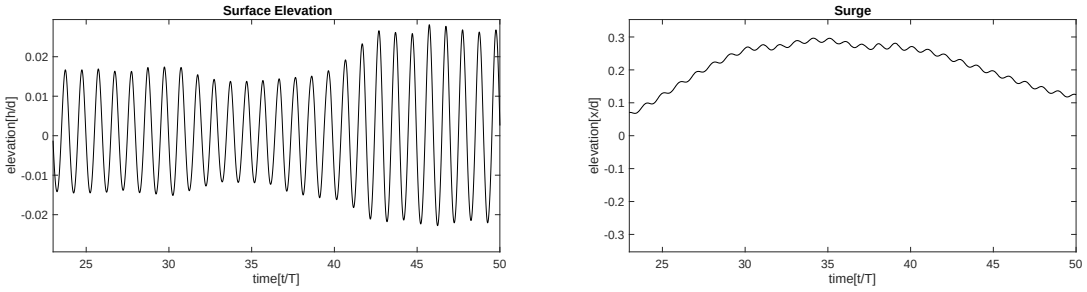

(a) (b) (c) (d)

Figure B.2: Long time modelled time series including springs (T = 0.8 s, H = 3cm)